CONSOLIDATION AND PERMEABILITY OF FLOCCULATED KAOLINITE SEDIMENTS

by

Jiawei Dong

A thesis submitted to the faculty of
The University of Utah
in partial fulfillment of the requirements for the degree of

Master of Science

Department of Metallurgical Engineering

The University of Utah

May 2017

The University of Utah Graduate School

STATEMENT OF THESIS APPROVAL

The thesis of **Jiawei Dong**

has been approved by the following supervisory committee members:

Jan D. Miller	, Chair	**June 1st, 2016** Date Approved
Chen-Luh Lin	, Member	**June 1st, 2016** Date Approved
Raj K Rajamani	, Member	**June 1st, 2016** Date Approved

and by **Manoranjan Misra** , Chair/Dean of the Department/College/School of **Metallurgical Engineering**

and by David B. Kieda, Dean of The Graduate School.

ABSTRACT

Clay mineral particles such as kaolinite (<2 microns in size), can cause significant problems in flotation processes and tailings disposal, including the processing of Florida phosphate rock and Canadian oil sands. In this thesis research, the sedimentation and consolidation of flocculated kaolinite suspensions are examined. High resolution X-ray Microtomography is used to describe the structure of the consolidated sediment. With this tomographic information, the complex geometry of the pore network structure for the consolidated flocs was established for the first time. With the experimental pore network structure, permeabilities were estimated by Lattice Boltzmann Simulation.

Results for kaolinite sediment with and without polymer were compared and discussed as well as the effect of centrifugal forces. Results for flocculated kaolinite sedimentation/consolidation in a gravitational field are presented and discussed; the results show that as the polymer dosage increases the permeability of the flocculated kaolinite sediment increases, and as the suspension pH increases, the permeability of the flocculated kaolinite sediment decreases. Results for flocculated kaolinite sedimentation/consolidation in a centrifugal field are presented and discussed as well; the results reveal that when the centrifugation time increases, the permeability of the flocculated kaolinite decreases. Finally, as expected when the centrifugal forces increase, the permeability of the flocculated kaolinite sediment decreases.

TABLE OF CONTENTS

LIST OF TABLES

Tables

ACKNOWLEDGEMENTS

First of all, I would like to acknowledge and express my deepest gratitude to my supervisor Dr. Jan D. Miller for his continuing support, excellent guidance, encouragement and continual technical and financial assistance throughout my time at the University of Utah. Without his patience, constructive criticism, and timely advice, this endeavor would not have been successful. Also, I would like to thank Dr. C. L. Lin for his invaluable help, time, and guidance during the entirety of my thesis research.

Secondly, I would like to thank Dr. Raj K. Rajamani for his positive response to be a member of my supervisory committee and valuable advice and comments on the thesis research. Moreover, I thank Dr. Alvaro R. Videla for his advice and suggestions about this thesis. I appreciate the University of Utah, the Department of Metallurgical Engineering in particular, for providing a pleasant and friendly environment that helped me through all the hard work.

Thanks to all my fellow colleagues in the research group and friends for their generous help and encouragement throughout my coursework and this research. Without their help, my stay and survival would be impossible.

Last but not least, I feel very much indebted to my parents and my family for their love, affection, and continuous support. Without their understanding, it will be impossible for me to travel so far away from home and pursue my degree.

CHAPTER 1

INTRODUCTION

This chapter introduces the problem statement for undertaking the thesis research topic selected for study, followed by research objectives, and the outline of the thesis.

1.1 Problem Statement

Vast oil sand resources are located in the province of Alberta, Canada, where water-based oil sands extraction operations are found. These operations include extraction and separation of the bitumen from the clay, sand, and water that make up the tar sands. The production of one barrel of synthetic crude oil (SCO) generates 1.8 tonnes of solid tailings and requires 2 m^3 of processed water [1]. While coarse solids (sands) settle quickly to form beaches along the tailings pond, the fines (mainly silts and clays) take a much longer time to settle. Even after a few years, solids remain suspended in the process-affected tailings water in the form of sludge that contains approximately 30% fine solids and about 70% water by weight. This sludge is known as mature fine tailings (MFT) or fluid fine tailings (FFT). At current bitumen extraction rate, the volume of MFT discharged increases at an alarming rate.

According to the Fine Tailings Fundamentals Consortium (FTFC), over 800, 000 tonnes per day (TPD) of tailings were discharged by Suncor and Syncrude in 1995 [2]. An estimation is that Syncrude will produce one million cubic meters of tailings by 2050 and

Suncor will discharge 800 million cubic meters by 2033. Currently, the total area of tailings ponds in Alberta has reached 130 km^2.

Continuous provision for the containment of mature fine tailings requires a direct incremental operating cost and has drawn great attention for major logistical and environmental concerns [3]. Great efforts have been made by many researchers to enhance treatment of mature fine tailings to increase the solid settling velocity and the rate of consolidation by optimizing the physicochemical conditions of the system. The oil sands feed material is composed of bitumen (~12%), sand, silts, clays (mineral content ~85 wt.%) and water (3-6 wt.%). The clay component is comprised mainly of kaolinite (50-60%) and illite (30-50%) with some montmorillonite [2, 4].

Kaolinite, a major clay mineral found in oil sand tailings, is a bilayer phyllosilicate each bilayer consisting of a silica tetrahedral sheet and an alumina octahedral sheet. In this way, kaolinite particles have three different surfaces: the alumina face surface, the silica face surface, and the edge surface. Gupta and Miller reported that the silica face surface is negatively charged from pH 4 to pH 10 while the alumina face surface of kaolinite has an isoelectric point at around pH 6, below which the alumina face is positively charged and above which it is negatively charged [5]. According to Liu et al., the edge surface of kaolinite is negatively charged from pH 4 to pH 9 [6]. The different dependence of kaolinite surfaces on suspension pH results in various states of aggregation of kaolinite particle suspensions depending on the system pH.

Organic polymers have been used to flocculate kaolinite to enhance the dewatering rate and allow fast compaction. However, the effect of flocculation of kaolinite is significantly influenced by the mixing conditions that must be adjusted to prevent over-

shearing of the polymer, breakage of the floc structures, and reduction in subsequent consolidation. In this way, recovery and reuse of water can be improved.

Flocculation and dewatering of kaolinite involve the growth of flocs, sedimentation, compaction/consolidation of solids, and water removal by drainage through the porous structure. An accurate assessment of the transport properties in the consolidated kaolinite is of great significance in the development of improved flocculation and dewatering processes for mature fine tailings. Currently, there is limited understanding of the fundamental phenomena involved at the pore-scale level, the level which controls the overall behavior of the flocculation and dewatering processes.

Several factors affect the flocculation and subsequent recovery of water including flocculant types (molecular weight, structure, and so forth), flocculant dosage, mixing conditions, and pH of the system. Understanding each factor and its effect is necessary to define the optimal conditions for flocculation and dewatering of kaolinite and eventually MFT. However, such a task is complicated and overwhelming since it entails a large group of variables, including the complexity of the pore geometry, which is difficult to determine experimentally. The approach currently used involves the direct quantification of the volume of water collected during sedimentation, or indirectly measuring the water drainage rate from a capillary suction test. Nonetheless, there is no linear or nonlinear rule for a combination of the active physical properties of the microscopic scale that can be used to predict the macroscopic level properties. The lack of a fundamental understanding of flocculation and the dewatering process at the pore-scale level limits the ability to predict and resolve common filtration problems such as cake cracking and moisture retention as well as water release during sedimentation. In this regard, it is important to introduce

appropriate experimental techniques and theoretical models to describe in detail at the pore-scale level the flow occurring through a packed bed of flocs during the flocculation, sedimentation, dewatering, and consolidation processes.

Understanding the fundamental parameters involved in the flocculation and dewatering process is essential to improve water removal and recovery. In order to gain a better understanding of the complex transport phenomena that occur in the sedimentation of flocs during consolidation and compaction, this research investigated the effect of three-dimensional pore geometry on the active transport properties of the consolidated kaolinite sediment.

1.2 Research Objectives

The main purpose of this research was to characterize and improve understanding of the dewatering properties of kaolinite using polymer modification in gravitational and centrifugal fields. The specific objectives were as follows:

- 3D imaging of sedimented kaolinite flocs using high-resolution X-ray microtomography (HRXMT), and based on image analysis, to obtain the geometric microstructure of the flocs and pore network structure (free water pathway) of sediments in gravitational and centrifugal fields.
- Permeability estimation from fluid flow through consolidated kaolinite by coupling the 3D HRXMT data with the Lattice Boltzmann Method (LBM) to simulate the water flow velocity.
- Correlate the microstructure of consolidated kaolinite with the preferred conditions for water recovery.
- Compare consolidation of flocculated kaolinite in a gravitational field and a

centrifugal field.

1.3 Thesis Outline

Chapter 1 introduces the problem statement for undertaking this thesis research topic as a study followed by the research objectives and the outline of the thesis.

Chapter 2 contains the literature review. It begins with the fundamentals of kaolinite clay, which consists of kaolinite structure, surface chemistry, and kaolinite flocculation mechanisms, followed by the bonding mechanisms between kaolinite and the polyacrylamide flocculant. Then, the review introduces the x-ray microtomography techniques, and the LBM used to simulate fluid flow through flocculated kaolinite sediment. Finally, the digital image processing techniques used for image analysis are explained.

Chapter 3 describes the materials and research methodology used for the laboratory testing of flocculated kaolinite in gravitational and centrifugal fields, including the preparation of flocculated kaolinite suspensions and polyacrylamide solutions, X-ray microtomography scans, estimation of permeability, pore network structure analysis, and feature based classification – ImageJ/Fiji and the Trainable Weka Segmentation (TWS) plugin for segmentation of sedimented flocs.

Chapter 4 presents the results for polymer flocculated kaolinite sediment in a gravitational field as affected by various suspension pH and polymer dosage conditions.

Chapter 5 reveals the results for polymer flocculated kaolinite sediment in a centrifugal field as affected by centrifugal forces and centrifugation time.

Chapter 6 summarizes the results and presents conclusions drawn from this research. The last section of this thesis consists of a list of references.

CHAPTER 2

LITERATURE REVIEW

The literature review begins with the fundamental features of kaolinite clay, which consists of kaolinite chemistry, structure, and surface chemistry. The review then discusses polymer induced flocculation of kaolinite. Finally, two geotechnical index properties used to compare the sediment structures of flocculated kaolinite are introduced.

2.1 Fundamental Features of Kaolinite Clay

2.1.1 Kaolinite Chemistry and Structure

Kaolinite is a bilayer phyllosilicate consisting of a tetrahedral silica sheet linked through oxygen atoms to an alumina octahedral sheet. Figure 1 shows the structure of kaolinite. The chemical formula for the kaolinite phyllosilicate mineral is $Al_2Si_2O_5(OH)_4$. In general, for phyllosilicate minerals the cationic ions may substitute the aluminum and silicon atoms, for example, Mg^{2+} or Fe^{2+} replaces Al^{3+} in the alumina octahedral layer and Al^{3+} for Si^{4+} in the silica tetrahedral layer [7]. However, for kaolinite the degree of substitution is not significant.

Consequently for kaolinite clay, the cation exchange capacity (CEC), at about five meq/100g, is low compared with other 2:1 type phyllosilicates like montmorillonite which has a CEC of 100 meq/100g [8, 9]. The replaceable $(OH)^-$ ions of the exposed alumina octahedral layer may contribute to the fact that the CEC of kaolinite is lower than its anion

exchange capacity [10].

2.1.2 Kaolinite Surface Chemistry

Because of the bilayer structure of kaolinite, composed of a silica sheet and an alumina sheet, kaolinite particles have three surfaces, the alumina face surface, the silica face surface, and the edge surface. Each kaolinite surface has a different surface charge. The distance between two repeating kaolinite bilayers is about 0.72 nm.

Recently, researchers reported the surface charge characteristics and wettability of the basal planes and edge surfaces of kaolinite [11–13]. Gupta and Miller [11] said the isoelectric point (IEP) of the alumina face surface of kaolinite is between pH 6 and 8, and the IEP of the silica face surface is below pH 4. In their study, individual kaolinite particles were ordered on substrates, and the prepared surfaces were confirmed by Atomic Force Microscopy (AFM) measurements to be the silica face and alumina face, respectively. Wettability of the two basal planes of kaolinite particles have been studied by Yin [12]. She found that the silica face surface of kaolinite particles is more hydrophobic than the alumina face surfaces. This finding was then confirmed by molecular dynamic simulation as well. Until recent years, there has been only limited research reporting on the characteristics of kaolinite edge surfaces. The point of zero charges (PZC) of the kaolinite edge surface is estimated to be pH 4.5 [10]. Liu et al. [6] prepared well-ordered kaolinite edge surfaces as an epoxy resin sandwich structure that had layered kaolinite particles in the center of the epoxy resin sandwich. They evaluated the surface charge of the kaolinite edge surfaces with a sharp silicon tip cantilever from AFM surface force measurements. The PZC of the kaolinite edge surface was determined to be below 4, which they believed to result from a less isomorphous substitution in the silica tetrahedral layer. The

characteristics of the kaolinite surfaces potential are plotted as a function of pH in Figure 2.

Aggregation of kaolinite particles to form clusters may occur due to the attraction of oppositely charged surfaces as described below and shown in Figure 3 [13]. The aggregation is evidently due to electrostatic attraction between positive edges and negative cleavage faces of adjacent kaolinite crystals and is referred to as "edge-to-face" aggregation [7]. After adding NaOH, hydrogen ions are lost from the edge faces by proton transfer, the number of positive charges decreases, and consequently, the attraction is reduced.

Edge-to-face aggregation is exhibited most readily in salt-free suspensions, and with monovalent counter ions. Aggregation occurs rapidly to form clusters, and sedimentation results in a relatively large sediment volume.

Face-to-face aggregation of kaolinite particles is best exhibited at high salt concentrations, and with di- or trivalent counter ions. Particles arrange themselves in lamellar fashion, face-to-face, to form clusters. Aggregation occurs rather less rapidly, and sedimentation volume of such cluster is smaller than edge-to-face aggregation.

Cluster formation from kaolinite suspensions was found at a low pH (pH 5); in contrast, kaolinite particles were well dispersed at a high pH (pH 8) according to Liu et al. [14]. Face-to-face aggregation with cluster formation is facilitated at pH 4-5. This distinguishing feature is mainly due to the anisotropic surface properties of kaolinite particles and their pH dependence.

2.2 Polymer Induced Flocculation of Kaolinite

2.2.1 Polymer Flocculation

Several studies show that long chain anionic high molecular weight polyacrylamides (PAM) flocculants work efficiently for improved dewatering, particularly in oil sands tailings [15]. High molecular weight polymer has been found effective in flocculating negatively charged clay particles since the polymer can extend further away from the particle surface after being adsorbed [16].

Since anionic PAM is negatively charged, the driving force for adsorption is hydrogen bonding between the amine (R-NH2) groups of the polymer and the silanol and aluminol OH- groups of the clay particle surface sites. The mutual charge repulsion between the carboxyl group (COO^-) of polymers and the hydroxyl group (OH^-) of clay particles allows minimal polymer adsorption and facilitates the bridging of hydrogen bonding functional groups due to increased polymer length [17].

Optimum flocculation occurs at an appropriate polymer dosage (PD) that can produce large flocs and is capable of withstanding moderate shear forces without rupturing [17]. Under dosage results in dispersion while excess dosage allows the polymer to saturate the particles and thus prevents the particle collision necessary for further attachment to the polymers [18].

When adding a polymer solution to a suspension being mixed, the collision between the particles might result in the formation of flocs. Moreover, too much shear or rotation can break up flocs and result in a decrease in effectiveness [19].

In the industries of water treatment, paper making, and screen printing, enormous amounts of PAM are used for clarification and filtration. PAM also has extensive

applications for the treatment of suspensions in the mining, metal, and ceramics industries. The SNF A3338 polymer used in this thesis is a 30% anionic PAM consisting of millions of acrylamide subunits. Figure 4 shows the chemical structure of anionic PAM. Anionic PAM has X nonionic groups and Y anionic groups. The value of X and Y determines the percentage of anionic charge of the PAM.

2.2.2 Polymer Adsorption by Kaolinite

Many researchers have widely studied the adsorption of PAM at kaolinite surfaces. Kim and Palomino [20] proposed three mechanisms by which PAM adsorbs at kaolinite surfaces. PAM interacts with kaolinite either through bonding with a nonionic PAM unit, a cationic PAM unit, or through charge neutralization.

Laird proposed that cation bridging (PAM-Ca-Clay) is the primary bonding mechanism between anionic PAM and clay mineral surfaces when calcium is present in solution. He also observed more effective flocculation between kaolinite and anionic PAM in calcium systems than in sodium systems. Moreover, much of the observed flocculation behavior can be explained by cation bridging between negatively charged sites on the clay surfaces and negatively charged carboxylate groups on the anionic PAM. Under acidic conditions, the protonated nonbridging aluminol groups on the alumina face surface and on the edge surface of kaolinite particles and electronegative functional groups on anionic PAM are hydrogen bonded. The lack of efficacy of anionic PAM for flocculating quartz even under acidic conditions indicates that little or no hydrogen bonding between silanol groups and electronegative moieties on the anionic PAM [21]. Anionic PAM is highly effective in the Na-acid-kaolinite system because of the interactions between anionic PAM and nonbridging aluminol groups $\left(> Al - OH^{-0.5}\right)$, which are present on the edge surfaces

of kaolinite particles. Nonbridging aluminol groups readily protonate in acidic environments. Charge neutralization of carboxylate groups on the anionic PAM and protonated nonbridging aluminol groups probably occurs under moderately acidic conditions (pH 5 to 7).

2.2.3 Sedimentation and Consolidation

In a classic thickener, the particle concentrations define three zones along the process: the classification region, the settling region, and the compression region. Moreover, continuous thickeners involve both a sedimentation and a consolidation step. Sedimentation is the settling of a particle, or suspension of particles, in a fluid due to the effect of an external force such as gravity, centrifugal force, or any other body force [22]. Terzaghi [23] described consolidation as any process that involves a reduction in the moisture content of saturated soil without replacing the liquid with air. When stress is applied the soil particles pack together tightly and reduce bulk volume. The magnitude of consolidation can be predicted in many ways [24]. In Terzaghi's classical method, he used oedometer test to determine soil compression index. Coe and Clevenger [25] were the first to recognize that the settling process of a flocculent suspension gives rise to four different and well-distinguished zones as illustrated in Figure 5. Mishler [26] was the first to show through experimentation that the rate slimes settle is different for dilute suspensions when compared to the rate of settling for concentrated suspensions.

Terzaghi consolidation theory [23] points out that when rocks are stressed, the fluid pressure of the rock is opposite to that of the internal pores and the stress is a direct result of all quantifiable changes in the soil (compression, deformation, shear resistance).

Kynch [27] presented his famous paper *A theory of sedimentation*, in which he

proposed a kinematical theory of sedimentation based on the propagation of sedimentation waves in the suspension with a basic assumption that the local solid-liquid relative velocity is only affected by the solids volumetric concentration.

In 1967, Gibson et al. [28] refined Terzaghi's theory to allow for large strain consolidation. Kynch's theory can be derived from Gibson's equation by assuming that no effective stresses are developed. Therefore, Kynch's theory works well only in the first stage of a sedimentation and consolidation process.

Concha and collaborators established in 1979 [22, 30] a heuristic theory of sedimentation based on the fundamental principles of mechanics, but with more or less degree of intuition and empiricism.

2.3 Geotechnical Index Properties-Permeability

In the field of fluid mechanics and earth sciences, researchers use permeability to measure the ability of a porous and unconsolidated material to allow fluids to pass through the structure [30]. The permeability of a medium relates to the porosity, the shapes of the pores in the medium, and their level of connectedness. High permeability allows fluids to move rapidly through rocks. The unit of measure for permeability is the Darcy, honoring the French Engineer Henry Darcy (1803-1858) who was the first to describe the flow of water through sand filters for potable water supply. Permeability is part of the proportionality constant shown in Darcy's law which correlates discharge (flow rate) and fluid physical properties to a pressure gradient applied to the porous media:

$$\kappa = \nu \frac{\mu \Delta x}{\Delta P} \tag{1}$$

where ν is the superficial fluid flow velocity through the medium in m/s, κ is the

permeability of a medium in m^2, μ is the dynamic viscosity of the fluid in $Pa \cdot s$, ΔP is the applied pressure difference in Pa, and Δx is the thickness of the bed of the porous medium in meters. In naturally occurring materials, permeability values range over many orders of magnitude.

Hydraulic conductivity is the proportionality constant specifically for water flow through porous media. Permeability is a portion of the hydraulic conductivity and is a property of the porous media only, not the fluid. Given the hydraulic conductivity for a subsurface system, the permeability can be calculated as follows:

$$\kappa = K \frac{\mu}{\rho g} \tag{2}$$

where κ is the permeability in m^2, K is the hydraulic conductivity in m/s, μ is the dynamic viscosity of the fluid in kg/(m·s), ρ is the density of the fluid in kg/m^3, and g is the acceleration due to gravity in m/s^2.

Suksun et. al [31] reported that all clayey soils have the same permeability ranging between 10^{-7} cm/s and 10^{-9} cm/s.

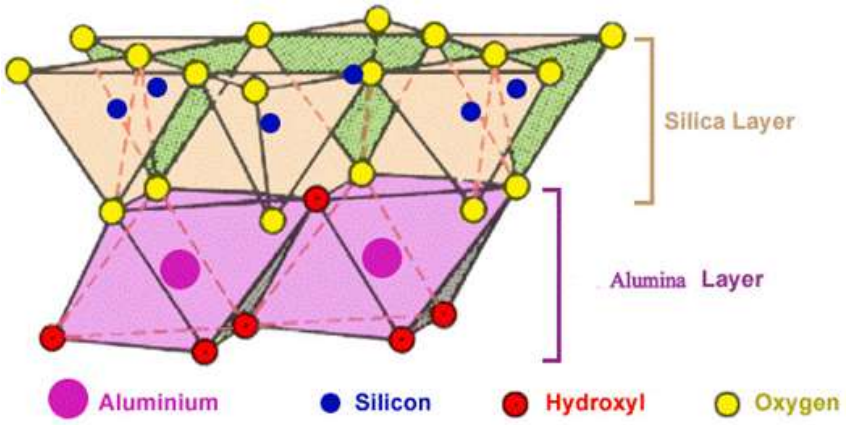

Figure 1: The structure of kaolinite.

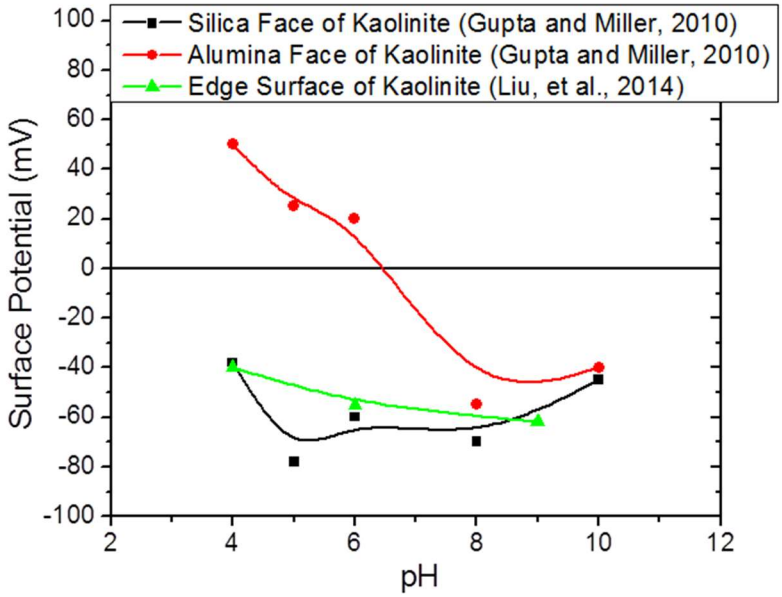

Figure 2: Surface potential features of kaolinite face surfaces as reported in the literature [6, 11].

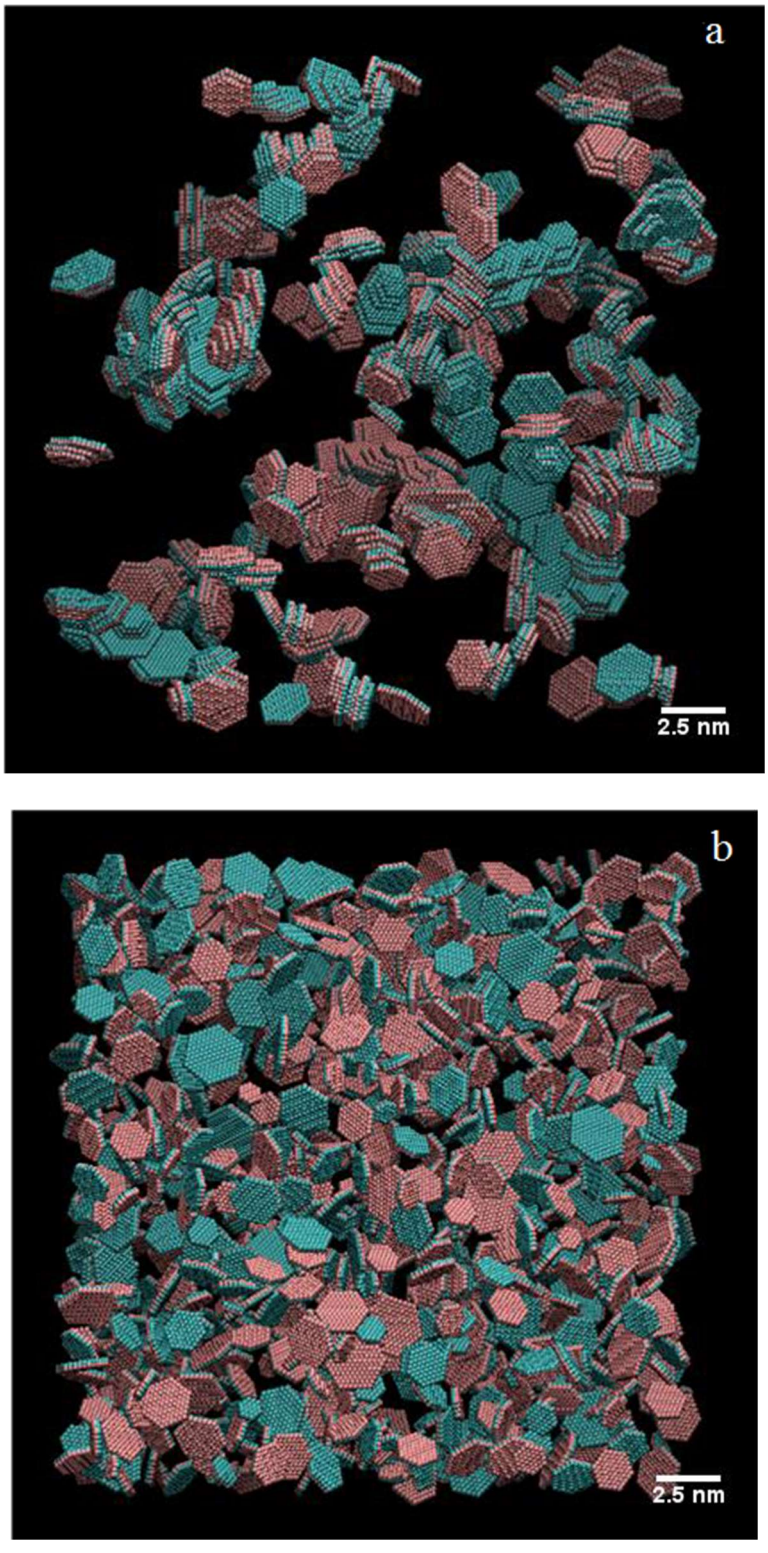

Figure 3: Brownian dynamics simulation snapshot of 1000 kaolinite particles after 10 ns simulation time at pH 5 (A) and pH 8 (B). Pink spheres represent the silica face surfaces of kaolinite particles, and cyan spheres represent the alumina face surfaces of kaolinite particles [13].

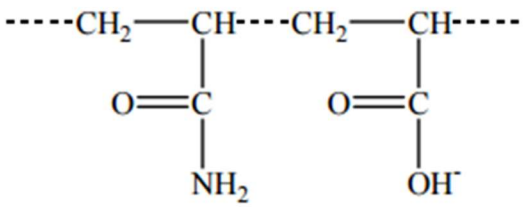

Figure 4: Chemical structure of anionic polyacrylamide (Stott et al.).

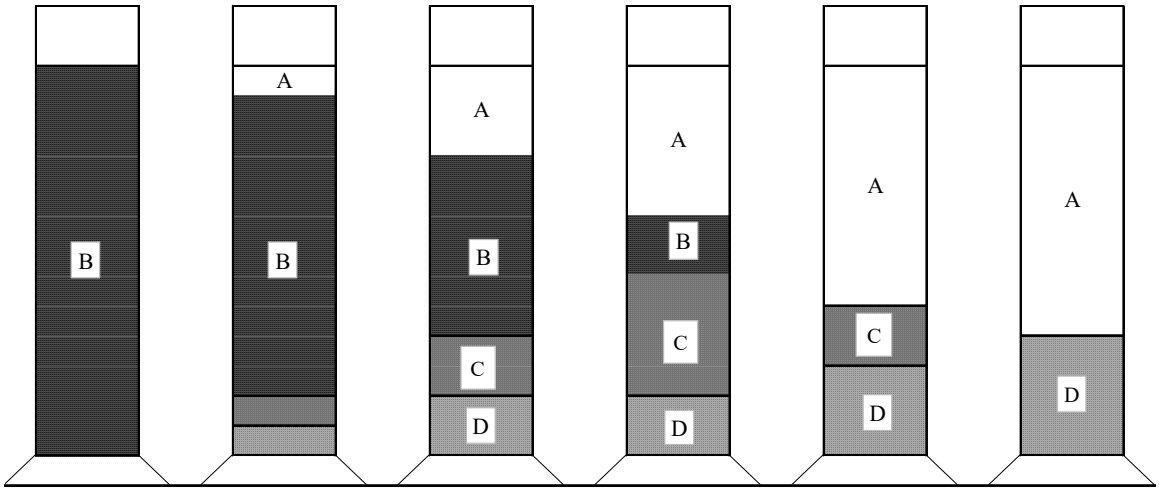

Figure 5: Settling of flocculated suspension as illustrated by Coe and Clevenger [25]. Figure shows the clear water zone (A), the zone in which the suspension is at its initial concentration (B), the transition zone (C), and the compression zone (D).

CHAPTER 3

MATERIALS AND METHODS

This chapter presents the research methodology for laboratory testing of flocculated kaolinite in gravitational and centrifugal fields. It includes the preparation of a polyacrylamide solution and flocculated kaolinite suspensions, X-ray microtomography scanning procedures, use of the TWS to process three-dimensional images of kaolinite sediment structures, and a description of the LBM procedure for the simulation of flow in the porous sediment structure of flocculated kaolinite.

3.1 Materials

In this study, the kaolinite used is acid washed kaolinite powder from Fisher Scientific, and its origin is from deposits in the United States. The catalog number is K2-500, and the lot number is 102664. This kaolinite clay was used without further treatment. The primary particle size distribution (PSD) of the dispersed kaolinite suspension is presented in Figure 6. Kaolinite suspensions were prepared in high purity Mili-Q water (Millipore Inc.). The resistivity of the deionized (DI) water was 18 MΩ-cm in all experiments. The polymer used is SNF A-3338 polyacrylamide (PAM), a 30% anionic PAM (SNF Holding Co.). Adjustments of suspension pH were made using 0.1 M HCl or 0.1 M NaOH solutions.

3.2 Kaolinite Consolidation Experiments

In this thesis study, 5% by weight of kaolinite suspensions were used for all the tests. During the preparation of each sample, 4 grams of kaolinite powder was weighed and mixed with 76 grams of DI water in a 150-ml beaker using a magnetic stirrer for one hour at a mixing speed of 700 rpm followed by half an hour of ultrasonic cleaning. Then the suspension pH was adjusted accordingly with the addition of HCl or NaOH.

The polymer concentration suggested by the supplier was 5 grams of polymer per 1 liter of DI water. SNF provided the powder flocculants preparation procedure for laboratory makeup of polymer solution. Limited by the amount of polymer solution required, this study used a 150-ml beaker to prepare the polymer solution. The polymer solution once prepared must be stored at a constant temperature between 5 °C and 30 °C. The freezing point of polyacrylamide is around 5 °C, and high temperatures will accelerate the aging of the polymer.

The preparation procedures for the PAM solution are as follows. First of all, 100 ml of polymer make-up water was prepared in a 150-ml beaker. Then, 4.000 +/- 0.005 g of powder flocculant was accurately weighed out onto a weighing paper. Next, start mixing the water at a frequency of 800 to 1000 RPM, using a magnetic stirrer bar in the beaker. After that slowly dust the powder polymer from the weighing paper into the vortex. If clumping occurs, begin entire procedure over again. After the polymer addition is complete, offset the mixer to provide turbulence and continue mixing for 30 minutes. The resulting solution should be clear and homogeneous. If fisheyes or globs of the polymer are evident, mixing should be continued until the solution is homogeneous.

A volume of polymer solution was measured with a micropipette before being

added to the kaolinite suspension. After pH adjustment of the kaolinite suspension, the polymer solution was introduced into the suspension while keeping the solution stirred at 500 rpm with a magnetic stirrer. Stirring continued for one minute. Then the slurry was transferred to a 25 dram (92 ml) cylindrical container with an inner diameter of 38.1 mm and a height of 83 mm as shown in Figure 7, after which the sample was allowed to settle for 24 hours before being scanned by HRXMT.

In the case of the centrifugation experiments, the flocculated kaolinite was allowed to settle for one day in a gravitational field before centrifugation. After flocculation and sedimentation using the same method mentioned previously, the sample was transferred to a centrifuge tube for centrifugal consolidation of the flocculated kaolinite. Then, for various conditions, the combined effects of centrifugation time and centrifugal force field were considered [32].

The Damon IEC HN-SII Centrifuge illustrated on the left of Figure 8 was used for all the centrifugation tests. The centrifuge is comprised of a swing bucket rotor with a 6-bucket capacity as shown on the right of Figure 8. It also allows the control of centrifugal time and rotation speed, which correspond to the control of different G-forces and centrifugation times. The centrifuge provides a maximum speed of 4900 RPM, maximum relative centrifugal forces (RCF) of 2750 x G, and maximum volume of 684 ml. An equal sample weight of around 80 grams was poured in each of the centrifugal tubes to ensure stability in rotation. The tests were conducted at a frequency of 1000 RPM to 4000 RPM and runtimes of 2 minutes to 8 minutes. Literature review and centrifuge capacity determined the frequencies and centrifugation times. The graduated tubes were retrieved after each test and put on the stand for visual observation and annotation.

The centrifugation tests used a 5% by weight kaolinite suspension at pH 6. The sample containers used during the centrifugal tests were Fisher brand 50-ml centrifuge tubes with an outer diameter of 30 mm and a length of 115 mm (Figure 9). Centrifugation factors like centrifuge time and centrifugal forces all affect the compactness of consolidated kaolinite sediments. The mixing of the kaolinite suspension took place in a 100-ml beaker before being transferred to the 50-ml centrifuge tubes. After applying a centrifugal field, the whole tube is plugged in a sample holder and mounted on the stage of HRXMT for scanning which requires 2.5 hours at a voxel resolution of 26.32 microns (Figure 10).

3.3 Methodology

The properties of fluid flow in porous media are significant for studies in oil recovery and contaminant remediation in aquifers. Normally, porous media are modeled as networks of pores or pore bodies that are connected via throats or channels. The flow velocity is influenced by properties of both the fluid and the pore network structure of the medium. Models like the LBM have been applied to simulate the flow process. These network flow models depend on several parameters that are supplied by experiments. Interpretation of experimental measurements of a porous medium property often is largely based on idealized models and equations. In contrast, the development of robust techniques for analysis of high resolution X-ray microtomography (HRXMT) images can provide direct quantification of geometric parameters for the pore space and fluid resident therein. Such results then serve as input to network models via parameter estimation [33].

Geometrical analysis of HRXMT images provides information on geometrical properties (and relationships between them) that are used as input to network flow models.

This geometric input is either in the form of the imaged network or regarding geometrically equivalent (in a stochastic sense) networks.

The cross-sectional dimensions of the pore space will in general not be uniform as one moves through the pore space. In particular, there may be narrow passages called pore throats separated by wide passages called pore bodies.

The points of direct interest in the flow through porous media are the properties of the pores (e.g., pore size distribution) rather than the properties of the matrix (e.g., particle size distribution). Important parameters of the pore space that relate to the trapping of fluids include the coordination number of the pores (e.g., the number of pore throats that branch out from a pore body) and the aspect ratio (e.g., ratio of pore body diameter to the pore throat diameter).

Methods introduced by Videla et al. [34], shown as a flowchart in Figure 11, were used to process 3D data and estimate permeability. In this approach, the kaolinite sediment was first scanned with HRXMT. Second, the HRXMT data was segmented in 3D using feature based classification instead of thresholding as the complexity of the sample made thresholding extremely inaccurate. Next, the pore network structures of the kaolinite sediments were reconstructed in 3D. Then, the LBM was used to simulate the fluid flow velocity distribution inside sediment channels. Finally, the permeability was estimated based on the average flow velocity.

The algorithms utilized in the analysis of the porous medium structure were void/solid phase segmentation, medial axis (MA) extraction and characterization, throat finding, the organization of the pore space into a network of pores connected by throats, and Lattice-Boltzmann-based pore and throat permeabilities computation as discussed in

more detail in the following sections.

3.3.1 High Resolution X-ray Microtomography Procedures

This thesis utilized the Zeiss/Xradia X-ray microtomography system (Model XCT400) with cone-beam projection. Cone beam reconstruction uses 2-dimensional projections for the construction of the 3D image. Instead of using a single row of detectors like fan beam methods, a flat panel detector is used for the cone beam system. It is referred to as cone-beam reconstruction because the X-rays produced from the point source travel as a cone-shaped beam. In other words, the X-rays originate from a "point" source and expand with distance from the source.

As illustrated in Figure 12, an X-ray source lines up with the detector, and the target object sits in between the source and detector. The target sample is rotated (see Figure 12), and projections are taken at each angular position.

Table 1 and Table 2 present two sets of HRXMT scanning parameters utilized to compare the sediment structures in a gravitational field and a centrifugal field. With these settings, the resolution or the voxel size in images obtained were 42.33 μm and 26.32 μm, respectively.

3.3.2 Image Segmentation – Feature Based Classification

The Trainable Weka Segmentation (TWS), one of the most used feature-based classification method, is an ImageJ [35] plugin that can be trained to learn from a set of user-input features and perform later the same task with an unknown data source. It not only makes use of all the powerful tools and classifiers from Weka but also classifies images based on a feature-trained classifier. A collection of machine learning algorithms

and a set of selected image elements are combined to produce voxel-based segmentations. Waikato Environment for Knowledge Analysis, also known as Weka, contains a collection of visualization tools and algorithms for the analysis of data and model development together with a user-friendly graphical user interface for easy access. There are several advantages of Weka. First of all, under the GNU General Public License, it is freely available to the public. Secondly, it runs on almost any modern computing platform as most of them fully implement the Java programming language. Thirdly, Weka has a comprehensive collection of data preprocessing and modeling techniques. Finally, a graphical user interface eases the use of Weka. Weka supports some standard data mining tasks like data preprocessing, clustering, classification, regression, visualization and feature selection. This plugin works as a bridge between the Machine Learning and the Image Processing fields. The framework is provided to use, and any available classifier is compared to perform image segmentation based on voxel classification by the Weka [36].

TWS [37] was used to segment tomographic images of flocculated kaolinite sediments. The process requires sample images to train the classifier which can then be used for the whole image stack to generate binary images as an input file for LBM Simulation. First of all, image features are extracted from an input image using Fiji-native methods. Next, a set of voxel samples is defined and represented as feature vectors, and a WEKA learning scheme is trained on those samples and finally applied to classify the remaining image data [37].

Figure 13 displays the user interface of TWS, where two characteristic features need segmentation. The solid phase and liquid phase are represented by red lines and green lines, respectively. Typically, several iterations of training and classifying will satisfy

segmentation requirements.

3.3.3 LBM to Simulate Flow in Porous Media

With parameters described in Table 1 and Table 2, each HRXMT scan generates a raw file that is 1012 by 1024 by 1014 voxels. With the binary input file segmented by TWS from the original HRXMT data, the LBM [38] was used to simulate fluid flow through the porous sediment structure and provide velocity distribution to calculate permeability. Maier et al. [39] used the LBM to simulate viscous fluid flow through a column of glass beads. The LBM used the digitalized porous structure for fluid flow simulation and determination of the local flow from which the macro flow properties for these complex geometries were obtained. Due to the insufficient sampling of the cone beam X-ray, around twenty layers at the top-most and bottom-most of the data are not usable as the image quality deteriorates as the distance from the center of the beam grows. Therefore, the first step of image processing was to remove those layers and a file of 300 layers of 400 by 400 voxels at the center was selected for each sample from the original HRXMT data. As illustrated in Figure 14, a 3D grid of voxels that contains the standard information for the kaolinite sediment has 300 layers along the Z-axis, and each layer has 400 by 400 voxels. To include enough features with a minimum number of voxel layers, five representative layers were chosen along the X-axis by a step of 100 layers for feature extraction and classifier training.

Then, the classifier was applied to all layers of the 3D image to generate a binary file where black represents a water-rich phase and white stands for a kaolinite-rich phase. Fluid flow along the Z-axis was then simulated by the LBM, and then the permeability was estimated based on simulated fluid flow velocity through the porous sediment structures.

Among the output of the LBM simulation, there is one file that contains the flow velocity distribution in the liquid phase. To obtain the flow channel network structure without the solid phase, this file was then used to subtract the segmented file and generate the 3D structure of fluid flow in the image calculator function. Before visualizing the water flow network structure, the ImageJ plugin Volume Viewer was used and the Look-Up Table (LUT) was changed from gray to 16 colors, which greatly enhanced the contrast of flow.

3.3.4 Pore Network Structure and Channel Flow

Microscopic pore space structure controls water transport in flocculated kaolinite sediments. Pore network structures represent the void space of a flocculated sediment in which constrictions of the pore channels account for the permeability of the sediment. Flow through the sediment can be described by LB simulation. HRXMT can be used to produce 3D image sets for samples of sediments such as kaolinite. These images, coupled with analysis software such as ImageJ, allows relatively rapid characterization of flocculated kaolinite sediments at the pore scale level. The LBM was used to compute an accurate approximation to Navier-Stokes flow through each isolated pore-to-pore connection in the sediments. In this way, connected channels from the top to the bottom are established using the connected components algorithm. Channels that are not connected through the sediment will not contribute to the flow through the sediments.

Lee et al. [40] presented an efficient three-dimensional (3D) parallel thinning algorithm for extracting both the medial surfaces and the medial axes of a 3D object (given as a 3D binary image). From the calculation of the medial axis for each of the flow channels, the distribution of channel diameters can be obtained. Figure 15 shows the skeleton of the

channels using a section of the 3D image as an example on the left. The Euclidean Distance Transform (EDT) map is shown on the right of Figure 15. The combination of these two images generates Figure 16 which is the medial axis map of this section and represents the spatial variation of the radii of channels according to grayscale level. Then the radii of the channels are converted to diameters in microns with the resolution of this image being 42.33 microns. The results are plotted in Figure 17. The largest channel diameter was found to be around 1.5 mm. The flow velocity distribution in LB units is shown in Figure 18.

Figure 19 shows the simulated three-dimensional spatial variation in velocity distribution with the color bar on the right indicating the magnitude of velocity at any particular location. The three-dimensional channel radius distribution is presented in Figure 20, and the color bar on the right indicates the magnitude of the channel radius. In this case, a maximum channel radius of 1.5 mm was found.

Connectivity is an important concept when flow problems are considered. Fluid flow can occur between two points only when the pore spaces are connected. In Figure 20, at the bottom left of the 3D image, there is a cluster that represents the existence of large channel sizes. However, high flow velocity is not observed in Figure 19 at the same location. This portion of channels is separate from the rest of the channels. They are not connected to other channels and are unable to transport water. In Figure 19, right above the bottom plane of the 3D image, a number of large channels has formed close to the lower part of the image while no high-velocity flow passes through the channels. These channels that are not connected do not contribute to the overall flow rate through the porous sediment structure.

Another problem with this method of using medial axis to obtain the radii of pores

is that it is based on the assumption that channels are cylindrical. The truth is that circular channels rarely exist in nature. The radius is represented by the distance from the point of measurement to the nearest black point. Therefore, it normally underestimates the size of the channels to some extent.

3.3.5 Permeability Estimation Based on LB Simulation Using HRXMT Data

Permeability defined by Darcy's Law is used to calculate permeability from laboratory measurement after some rearrangement. Traditionally, the measurement of permeability utilizes an equipment setup as illustrated in Figure 21 by forcing a fluid through the porous structure and recording the resulting fluid flux and pressure drops. The flow rate (Q) passing through a porous medium is directly proportional to the cross-sectional area (A) and hydraulic conductivity (K), directly proportional to the difference in the piezometric head ($\Delta h = h_1 - h_2$), and inversely proportional to the length of the sample (L). A general formulation of Darcy's Law is given as [41]:

$$Q = KA\frac{(h_1 - h_2)}{L} \tag{3}$$

$$h_i = z_i + \frac{p_i}{\rho g} \tag{4}$$

$$K = \frac{kg}{\nu} \tag{5}$$

The LB method is used to simulate the process shown in Figure 21 and calculates the average flow velocity and porosity. With the other known constant in the formula below, the permeability of the porous media can then be computed.

$$k = \frac{a^2 \nu \phi \bar{U}}{\rho g} \tag{6}$$

The permeability (k) is measured when the steady state is reached after the simulation is run through 5000 iterations. At that point the velocity achieves convergence. The permeability, in real physical units, is then proportional to the average velocity $\left(\bar{U}\right)$, the porosity of the medium $\left(\phi\right)$, and the kinematic viscosity of the fluid $\left(\nu\right)$. It is inversely proportional to the density of the fluid (ρ) and gravitational acceleration (g).

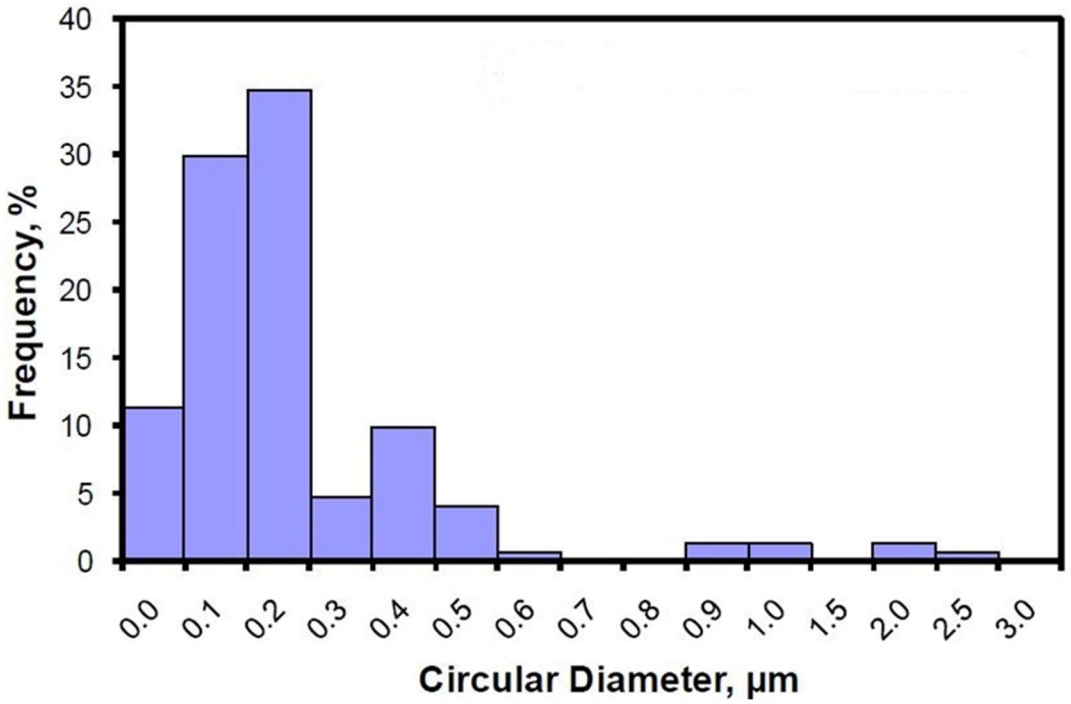

Figure 6: Particle size distribution of kaolinite [10].

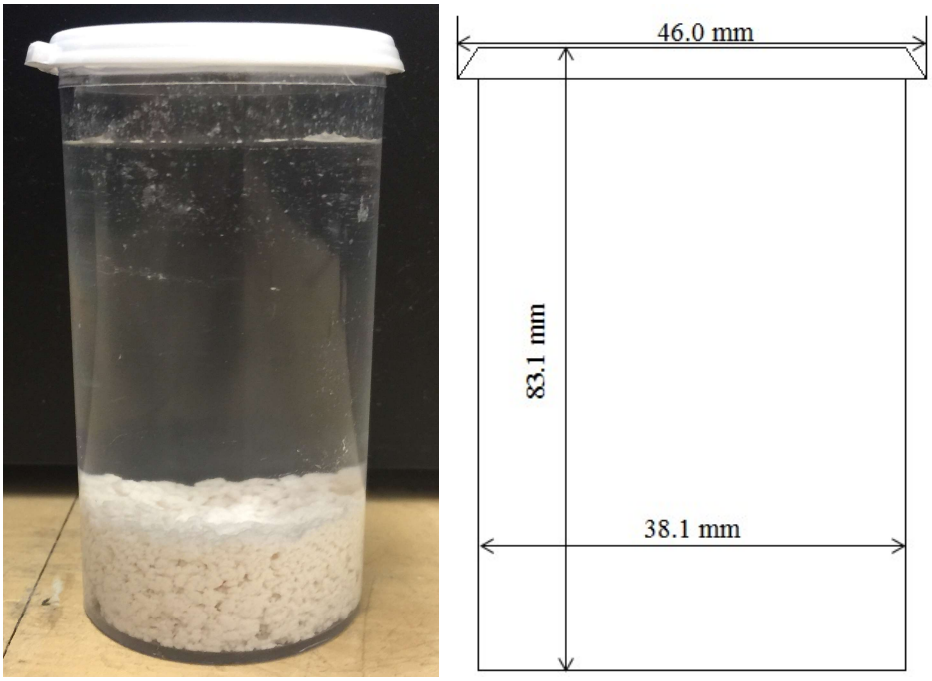

Figure 7: Cylindrical sample container (92 ml) used for flocculated kaolinite samples (left) and its dimensions (right).

Figure 8: The Damon IEC HN-SII Centrifuge (left) and the swing bucket rotor (right) used in this thesis.

Figure 9: The Fisher brand 50-ml conical bottom centrifuge tube (outer diameter 30 mm and length 115 mm).

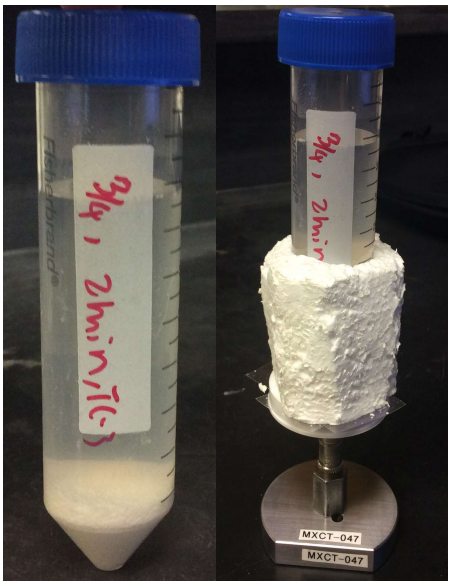

Figure 10: Centrifuged kaolinite sediment in a 50-ml centrifuge tube (left) and clamped in the sample holder (right).

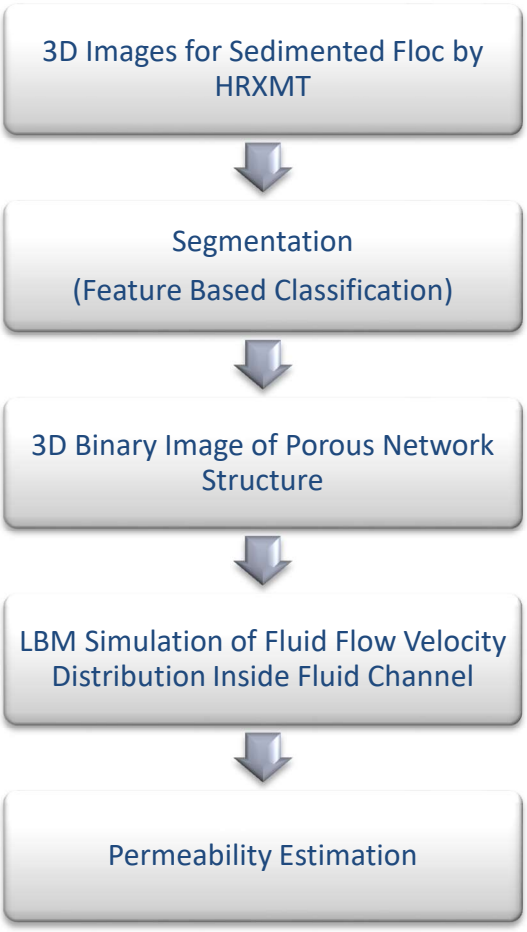

Figure 11: Flowchart of permeability estimation based on LB Simulation using HRXMT data [34].

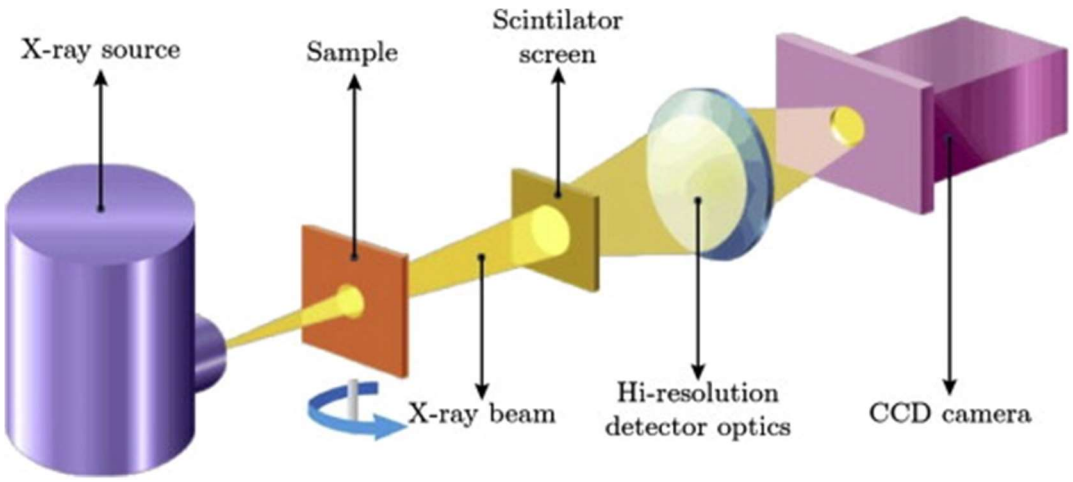

Figure 12: Schematic of X-ray microtomography system, Zeiss/Xradia (XCT-400).

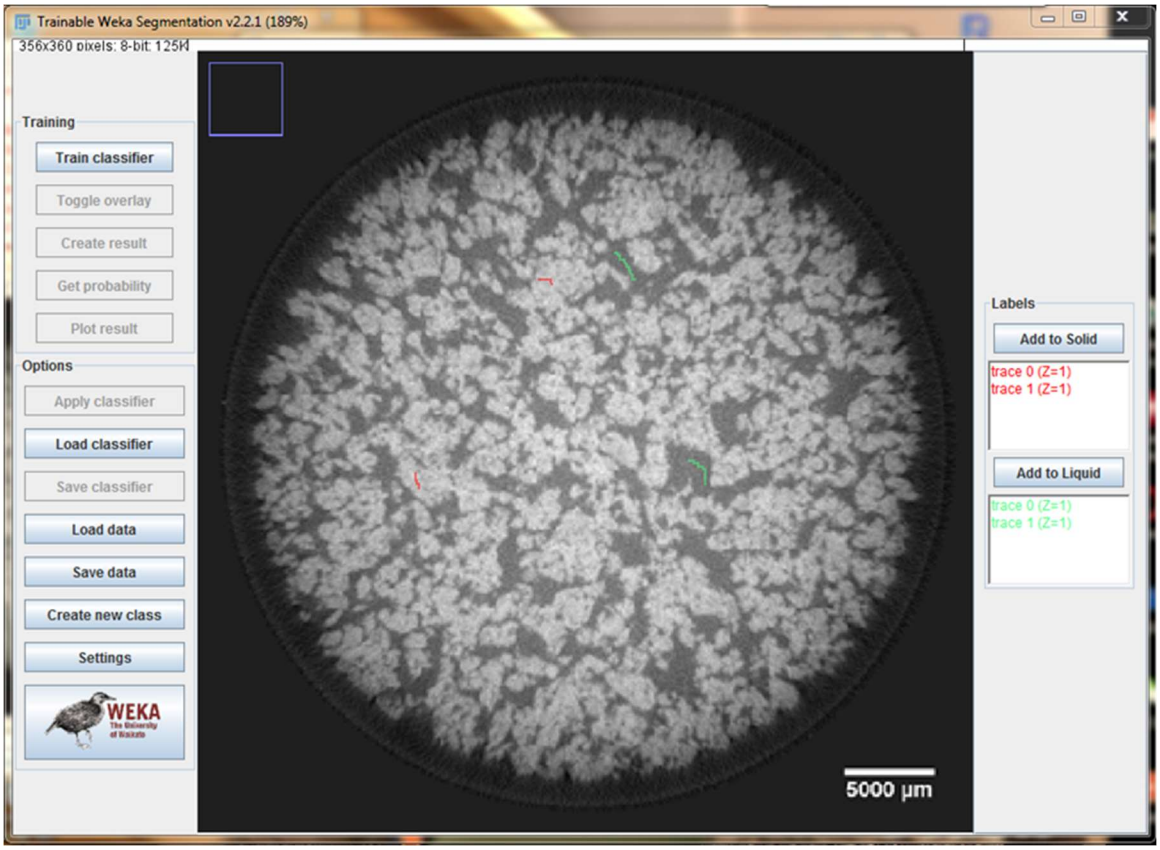

Figure 13: Trainable Weka Segmentation user interface.

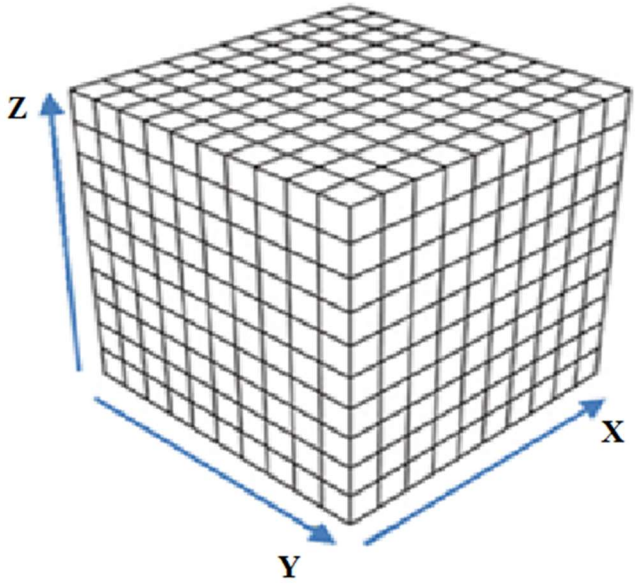

Figure 14: Volume data set – a 3D grid of voxels.

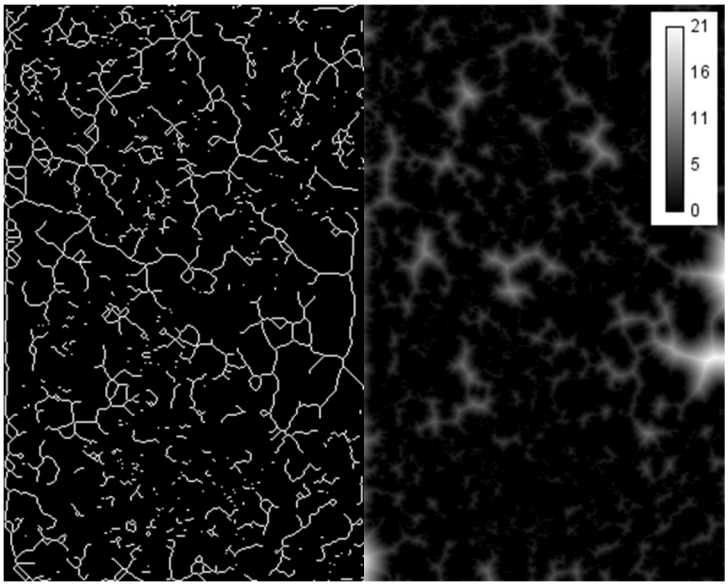

Figure 15: Skeleton map and distance map for the calculation of medial axis map. Channel skeleton for a selected layer of data on the left. On the right is the distance transformation map.

Figure 16：Medial axis map.

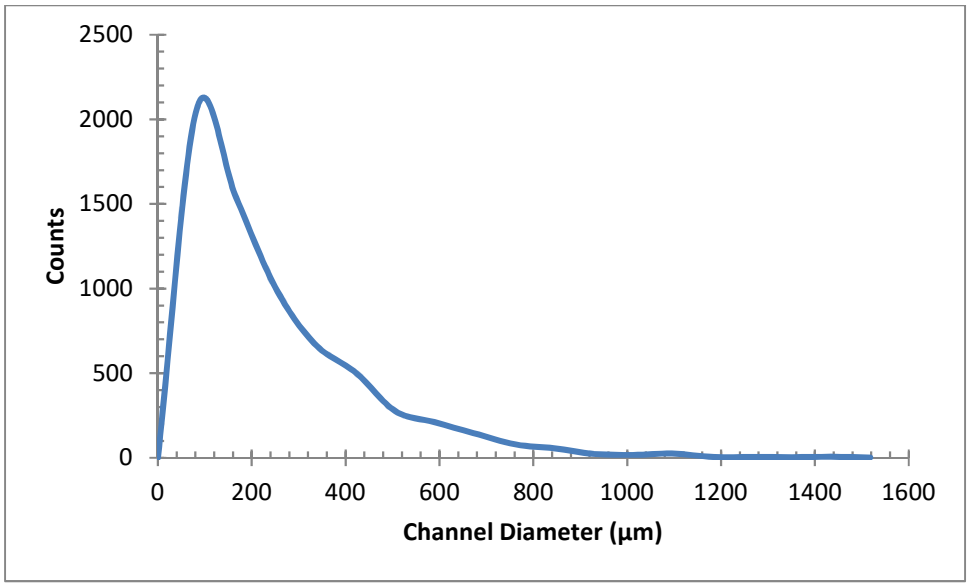

Figure 17：Channel diameter distribution.

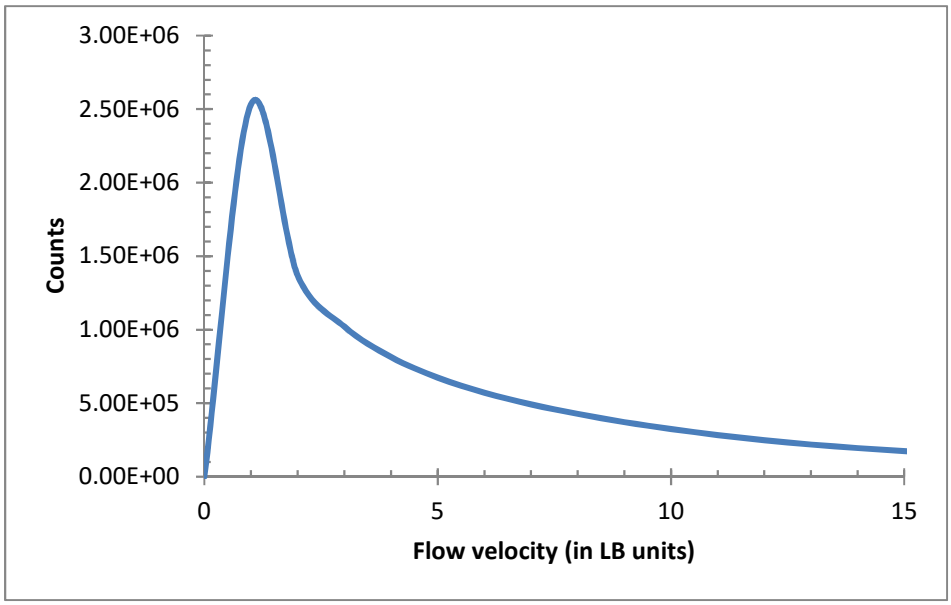

Figure 18: Flow velocity distribution in LB units.

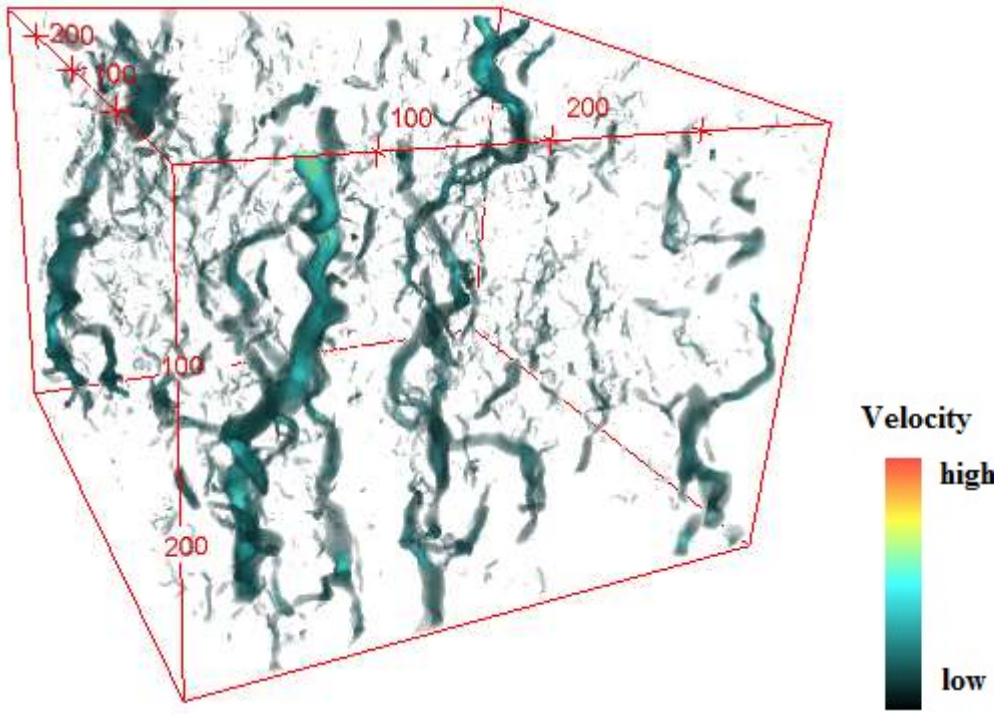

Figure 19: Flow distribution shown in 3D.

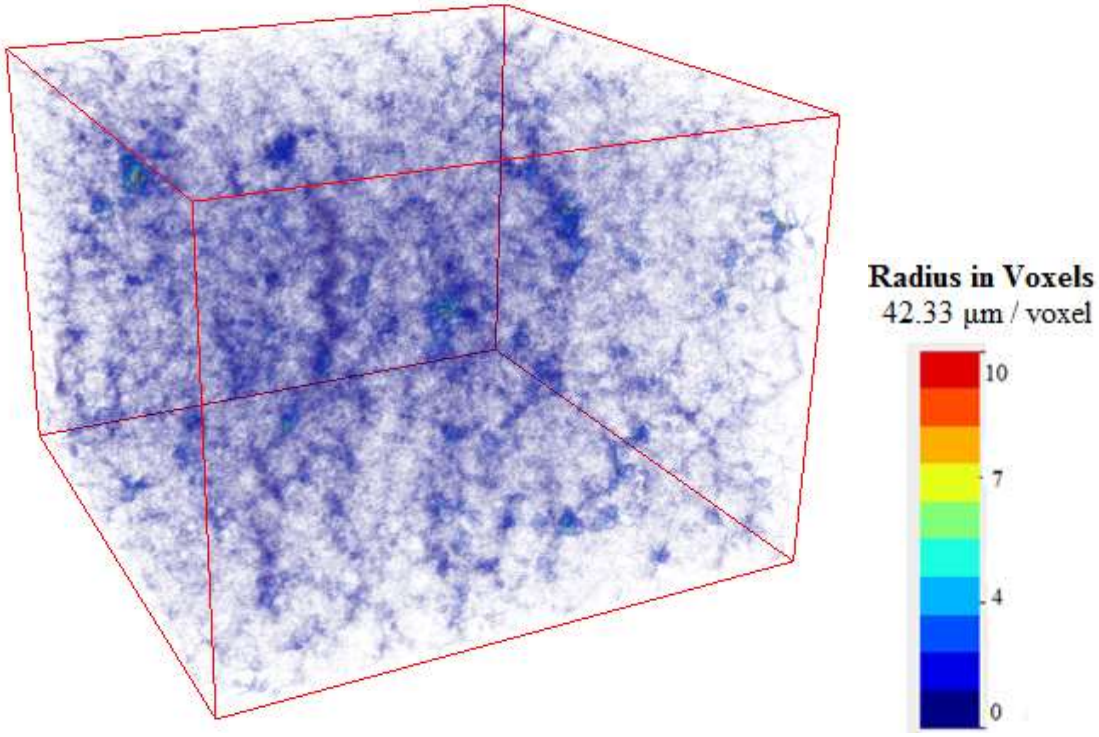

Figure 20: Medial axis in 3D.

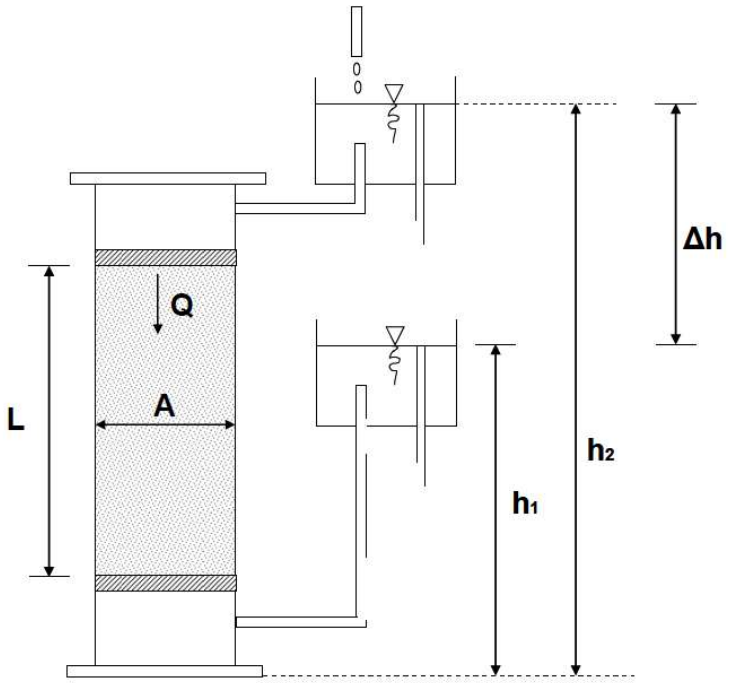

Figure 21: Darcy's experiment.

Table 1: Key HRXMT parameters for scanning flocculated kaolinite sediments in a gravitational field.

Total Scan Time	4 hours 6 minutes
Objective	0.5X
Source Settings (kV/W)	40kV/ 10 W
Pixel Size (μm)	42.33
Start and End Angle	-180/180
Number of View	1000
Time per View (sec)	10
Source / Detector Positions	-320/100 mm
Camera Binning	2

Table 2: Key HRXMT parameters for scanning flocculated kaolinite sediments in a centrifugal field.

Total Scan Time	2 hours 26 minutes
Objective	0.5X
Source Settings (kV/W)	40kV / 10 W
Pixel Size (μm)	26.32
Start and End Angle	-180/180
Number of View	1000
Time per View (sec)	4
Source / Detector Positions	-90/100 mm
Camera Binning	2

CHAPTER 4

SEDIMENT STRUCTURES IN A GRAVITATIONAL FIELD

This chapter presents the HRXMT images and their analysis to describe pore network structure, the LBM simulation of water flow, and the estimated permeability of polymer flocculated kaolinite in a gravitational field as affected by suspension pH and polymer dosage.

4.1 Effects of pH

One factor that affects the structure of the flocculated kaolinite sediment in a gravitational field is the suspension pH. The effect of suspension pH on the structure of flocculated kaolinite sediment originates from the surface charge characteristics of the kaolinite surfaces and the interaction of such surfaces with dissolved polymer molecules. Cross-sectional HRXMT images of flocculated kaolinite are shown in Figure 22 for a polymer dosage of 500 g/t at suspension pH values of 6, 7, 8, and 9. The diameter of the container is around 4 cm and images are at the same height from the bottom of the container. The brighter regions in the images represent regions rich in kaolinite (kaolinite flocs), and the darker gray regions represent water with few kaolinite particles. When comparing these cross-sectional images of flocculated kaolinite at different suspension pH values, one can easily see from Figure 22 that as the suspension pH increases, the size of the water-rich phase in the image decreases. The results at polymer dosage 500 g/t are an example to show

the trend, and this trend exists for all polymer dosages tested. Another phenomenon observed is that as the suspension pH increases, the size of the flocculated kaolinite decreases, which may be a combined result of kaolinite surface charge characteristics, flocculation mechanism between kaolinite particles, and the nature of polymer adsorption at surfaces of the kaolinite particles.

The isoelectric point of the kaolinite alumina face surface is between pH 6 and pH 7, therefore, at suspension pH 6, one can assume that the alumina face surface of kaolinite possesses positive charges while the silica face surface and edge surface are all negatively charged. Then some of the kaolinite particles flocculate with each other through both face-to-face flocculation and edge-to-face flocculation and, therefore, form a cardboard structure, which is more porous than face-to-face flocculated kaolinite particles. The anionic PAM used has noncharged units and anionic units, both of which can bond with kaolinite surfaces and form distinct kaolinite clusters. The sizes for kaolinite flocs at pH 6 and pH 7 are similar, as can be observed from the images.

At suspension pH 8 and pH 9, the size of the kaolinite flocs is much smaller than at lower pH values. Under these conditions the three kaolinite face surfaces are all negatively charged, and the kaolinite particles repel each other. Considering the bonding mechanism between kaolinite particles and anionic PAM proposed by Laird [21], the primary bonding mechanisms between anionic PAM and kaolinite is cation bridging (PAM-Ca-Clay). His flocculation data also suggest the existence of hydrogen bonding and hydrophobic bonding, of which the former is between electronegative units on the PAM and protonated nonbridging aluminol groups on edge surfaces of kaolinite, and the latter is between the carbon chain of the anionic PAM and basal surfaces of kaolinite. With no calcium ion

reported in the kaolinite suspension, cation bridging is rare at pH 8 and pH 9. The forces of hydrogen bonding and hydrophobic bonding are much weaker than cation bridging. Therefore, only small kaolinite flocs form. In contrast, at lower pH levels anionic PAM is highly effective in the Na-acid-kaolinite system because of the interactions between anionic PAM and nonbridging aluminol groups ($> Al - OH^{-0.5}$), which are present on the lateral edges of kaolinite. Sodium ions come from the use of NaOH during pH adjustments in this research.

4.1.1 Pore Network Structure

The suspension pH contributes to the pore network structure formed by the sediments of flocculated kaolinite aggregates. The pore diameter distribution was determined by the medial axis analysis technique. The pore diameter distributions by number are plotted in Figures 23 to 27 for flocculated kaolinite sediments at various pH values. Without the addition of the polymer, the pore diameters of kaolinite sediments are only a few pixels, and the results are limited by the resolution of the HRXMT. From pH 7 to pH 9, the largest pore diameter decreases at polymer dosage 0 g/t and 250 g/t. The largest pore diameter tends to decrease as the pH value increases for a polymer dosage of 500 g/t to 1000 g/t.

The pore network structure and flow velocity are correlated through Darcy's Equation which shows that larger pore size leads to higher flow rates for a given pressure drop. Figure 28 and Figure 29 show the spatial distribution of pore radius, determined by distance map transformation and skeletonization, for flocculated kaolinite sediments with 250 g/t polymer dosage at pH 7 and pH 8, respectively. The pore radius distributions indicate that the flocculated kaolinite sediment at pH 7 has larger channels. Comparing

Figure 28 with Figure 29, under the same color scale, one can see that as the pH increases, there are more and thinner channels at pH 8, most of which are well connected. The connectivity of the channels is one of the key factors that affects permeability of the sediments. The sediment at pH 8 and polymer dosage 250 g/t does not have large pore diameters, but instead those well-connected thinner channels contribute to the permeability of the sediment.

4.1.2 LB Simulation of Water Flow

The flocculated kaolinite sediments form pore network structures as described in 4.1.1 and the variation in these structures at different conditions determines the flow characteristics. The LBM simulation of fluid flow in porous media has been described by Lin et al. [38] and the same software was used to determine water flow through the sediment. From the simulated flow the permeability can be calculated. The flow velocity distribution shown in Figure 30 and Figure 31 confirms the existence of a higher velocity of flow at pH 7 than at pH 8 as predicted by the spatial distribution of pore radius at pH 7 and pH 8 and the polymer dosage is 250 g/t as shown in Figure 28 and Figure 29.

Figures 32 to 35 show simulated three-dimensional fluid flow from pH 6 to 9 at a polymer dosage of 500 g/t. The polymer solution contains 2.5 g polymer powder per 1 liter of deionized water. In these data, the amount of polymer (dosage) is expressed as gram polymer per ton of kaolinite. The color bar shown at the lower right of the figure indicates the flow velocity represented by various colors, where the velocity increases when the color changes from black to red. The unit of the flow velocity uses LB simulation lattice units (lu) instead of SI units. After removing the solid phase in the sediment, the water channels represented by the LB simulated flow are shown in Figure 36.

4.1.3 Permeability

When the fluid flow is simulated using the LB method, average flow velocity and porosity can be used to estimate permeability of the porous medium using equation (6). The permeabilities of the flocculated kaolinite sediments were estimated at various polymer dosages and suspension pH conditions. The estimated permeabilities also confirm the effect that suspension pH has on the sediment structure of flocculated kaolinite. Figure 33 plots the estimated permeability for different suspension pH values and polymer dosages and permeability values are listed in Table 3. It is evident that at all polymer dosage conditions, the permeability of flocculated kaolinite sediments decreases as the suspension pH increases and at higher polymer dosages, the estimated permeability decreases faster. Without the polymer addition, shown as the blue curve at the bottom, the permeability does not change much with change in pH, probably due to the HRXMT resolution limit. The primary kaolinite particles are less than two microns in size, and the kaolinite cluster size is much smaller than the voxel resolution of 42.33 microns without the polymer addition. At high pH values, particles are well dispersed and flocculation between particles and polymer is reduced. Clusters formed are too small to be detected by the HRXMT system.

4.2 Effects of Polymer Dosage

The other factor that affects the flocculated kaolinite sediment in a gravitational field is polymer dosage. Sediments at various pH and polymer dosage conditions have been scanned with HRXMT. Figure 37 shows cross-sectional images at the same depth for samples at pH 6 and polymer dosages of 0, 250, 500, 750, and 1000 g/t of kaolinite, respectively. Without any polymer addition, the kaolinite suspension itself consists of fine kaolinite particles (< 2 microns) that aggregate with each other either through face-to-face

connection or face-to-edge connection and form clusters that are 100 to 150 microns in size at pH 6. As the polymer dosage increases in 250 g/t increments, the interaction between kaolinite face surfaces and PAM units increases since more polymer bonding sites are available in the system. The larger size of this water-rich phase is seen in the cross-sectional views in Figure 37.

4.2.1 Pore Network Structure

Based on the 3D data of flocculated kaolinite sediments, the pore network structures that were obtained through segmentation using the Trainable Weka Segmentation program, and the pore diameter distribution of flocculated kaolinite sediments at various polymer dosage conditions obtained through medial axis analysis on the segmented images are presented in Figures 38 to 41. The analysis of the largest diameter presented in these figures reveals that the polymer is more effective at lower pH values. When the polymer dosage increases from 0 to 500 g/t the largest pore diameter increases at pH 6, pH 7, and pH 8. After polymer dosage reaches 500 g/t, pore diameters do not increase at pH 6 and pH 7. At pH 9, the pore diameter varies, and the largest pore diameter (about 460 microns) shows up at 250 g/t polymer dosage. This can be correlated with the fact that at this pH value kaolinite particles repel each other and form large amounts of small pores and throats in the sediment structures. The size of these challenges the resolution of the HRXMT.

4.2.2 LB Simulation of Water Flow

The pore network structures of flocculated kaolinite sediments determine the various fluid flow characteristics at different conditions that have been simulated with the LBM. Figures 42 to 46 show the LB simulated fluid flows at pH 6 and different polymer

dosages. The color bar shown on the right side of each image represents increasing water flow velocity from dark to red. Without the addition of polymer, the primary bonding mechanism is the bonding between kaolinite particles, which includes face-to-face and face-to-edge connection at pH 6. As the polymer dosage increases, small flocculated kaolinite aggregates start to appear. As more polymer is added to the system, the size of kaolinite aggregates keeps increasing. The adsorption of PAM by kaolinite particles releases the water content of the flocs.

4.2.3 Permeability

From the simulated LBM flow through flocculated kaolinite sediments, the average flow rate can be determined and the permeability estimated. The experiments on the sedimentation of flocculated kaolinite in a gravitational field considered two factors that affect the sediment structure: the polymer dosage and the suspension pH. Using equation (3), Table 3 presents the calculated estimation of permeability for flocculated kaolinite sediments in a gravitational field at different suspension pH values and polymer dosages. Figure 47 plots the permeability at various conditions from the perspective of polymer dosage. From the plot, one can see that without the addition of polymer, the permeability of kaolinite sediment at different pHs are similar as particle sizes are around 6 microns, which is below the resolution of the image. When the polymer dosage increases, the permeability increases at different suspension pHs. With lower suspension pH, the permeability tends to increase faster. Without the addition of polymer, due to the limitation of the voxel resolution of the HRXMT system, particles are too small to be detected and differentiated, the permeabilities at four different pH conditions are almost the same.

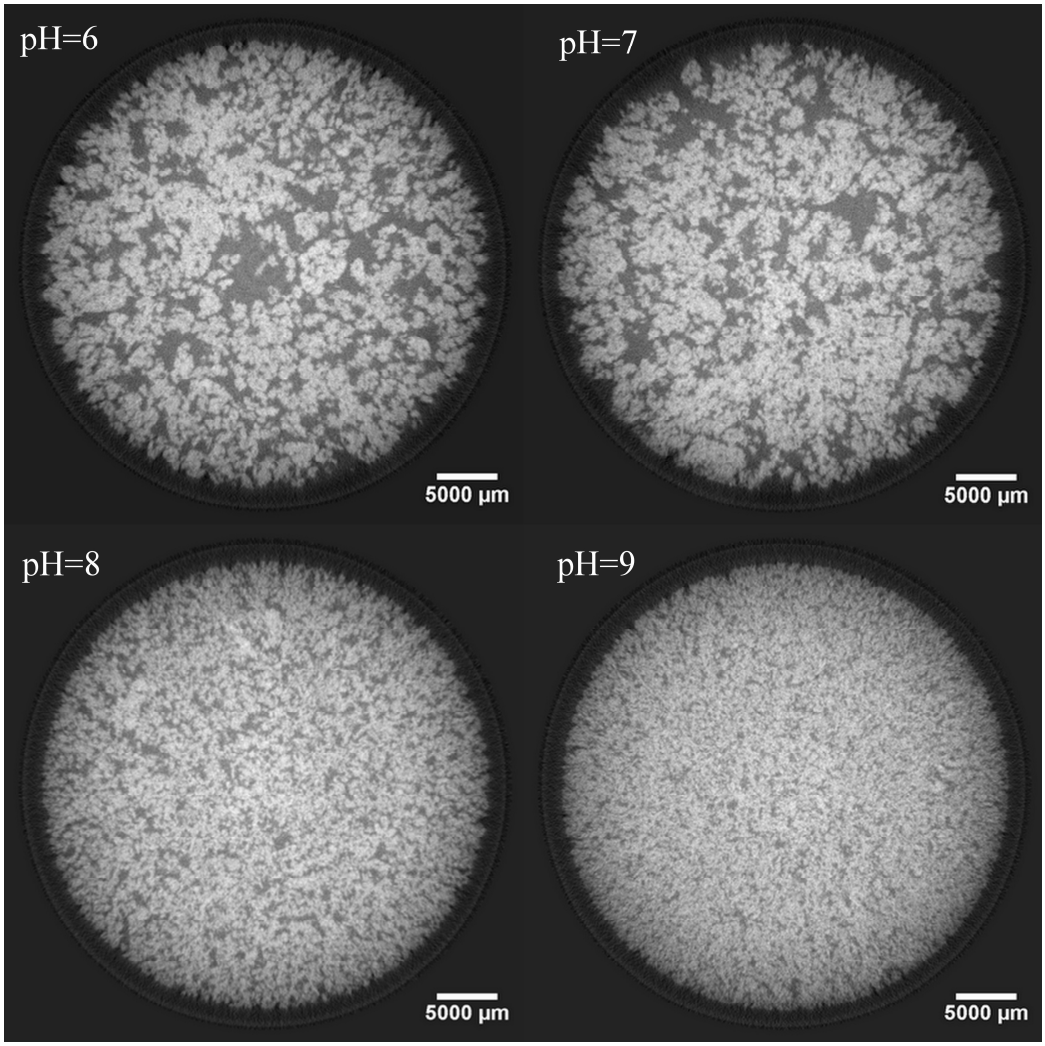

Figure 22: Cross-sectional images at the same depth for samples with 500 g/t polymer dosage at suspension pH values of 6, 7, 8, and 9.

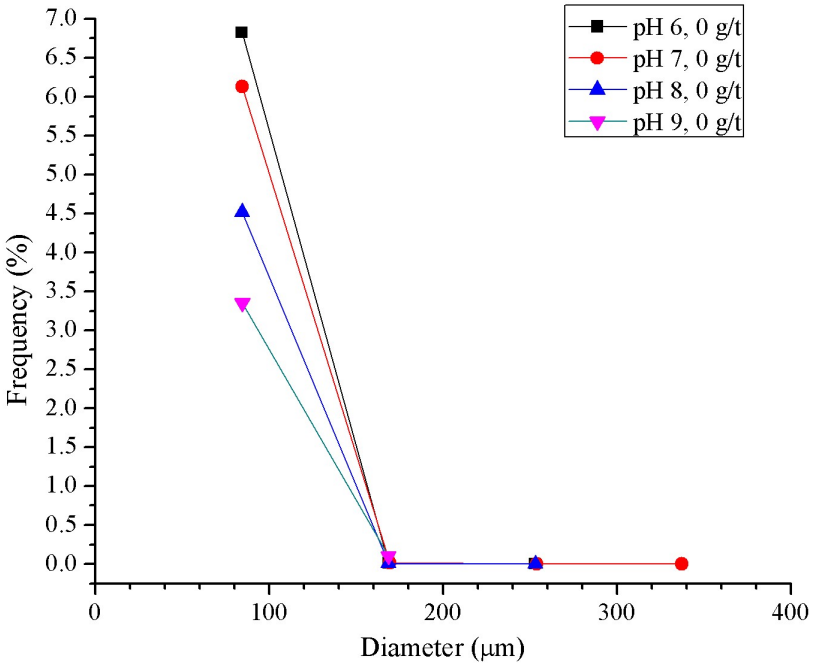

Figure 23: Pore diameter distribution at polymer dosage 0 g/t.

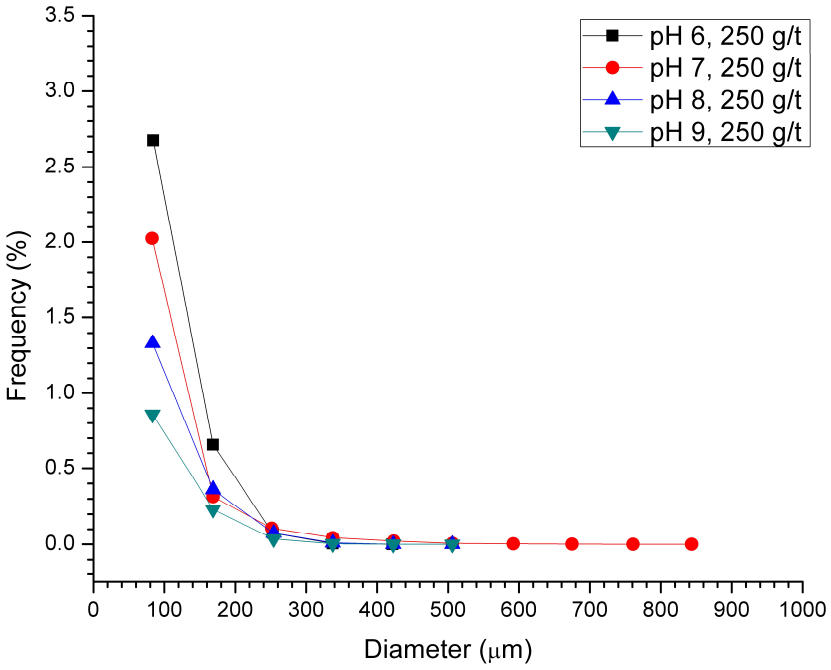

Figure 24: Pore diameter distribution at polymer dosage 250 g/t.

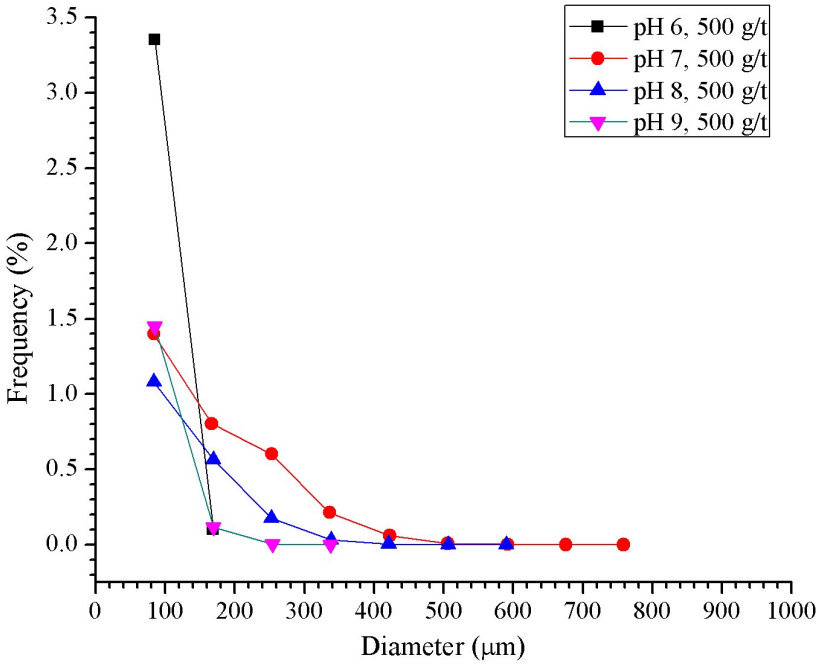

Figure 25: Pore diameter distribution at polymer dosage 500 g/t.

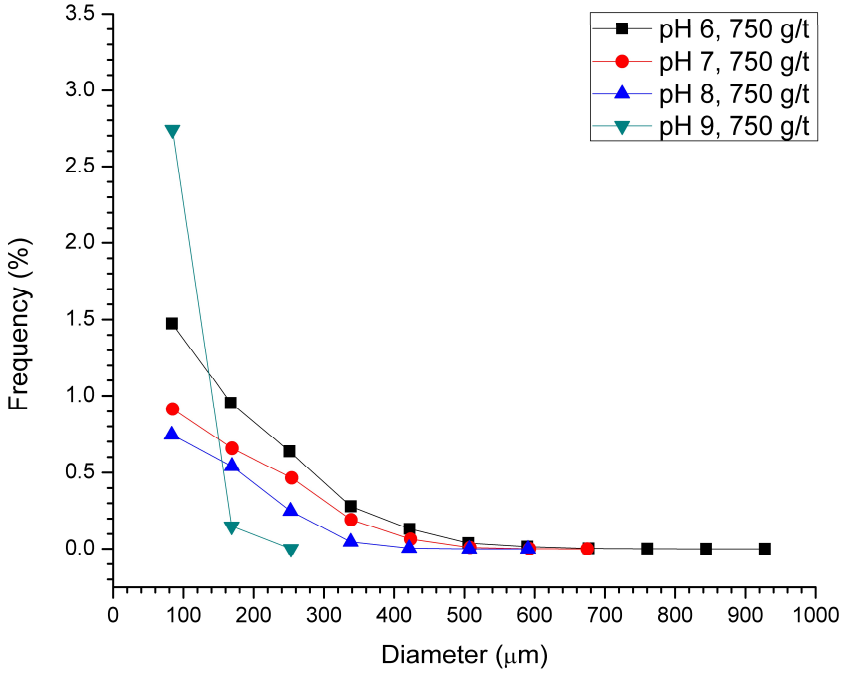

Figure 26: Pore diameter distribution at polymer dosage 750 g/t.

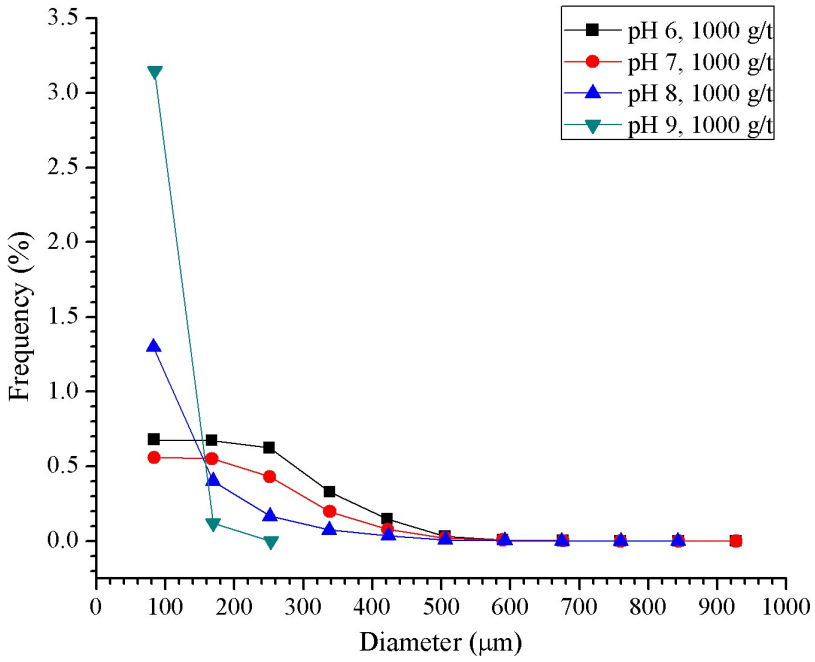

Figure 27: Pore diameter distribution at polymer dosage 1000 g/t.

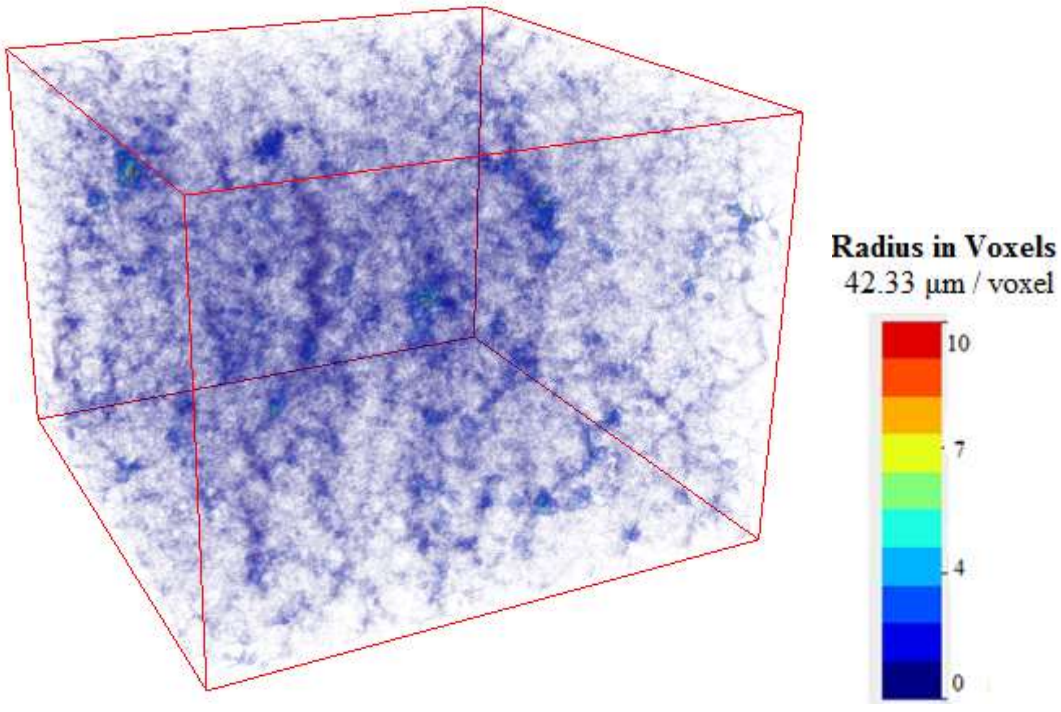

Figure 28: The spatial distribution of pore radius at pH 7 and polymer dosage 250 g/t.

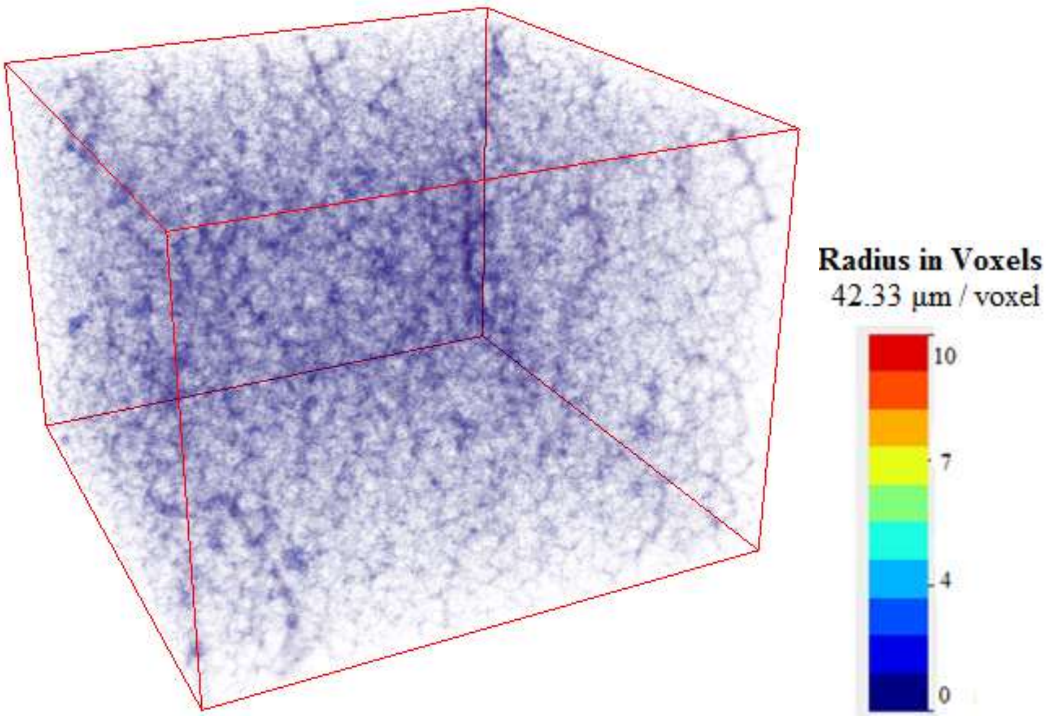

Figure 29: The spatial distribution of pore radius at pH 8 and polymer dosage 250 g/t.

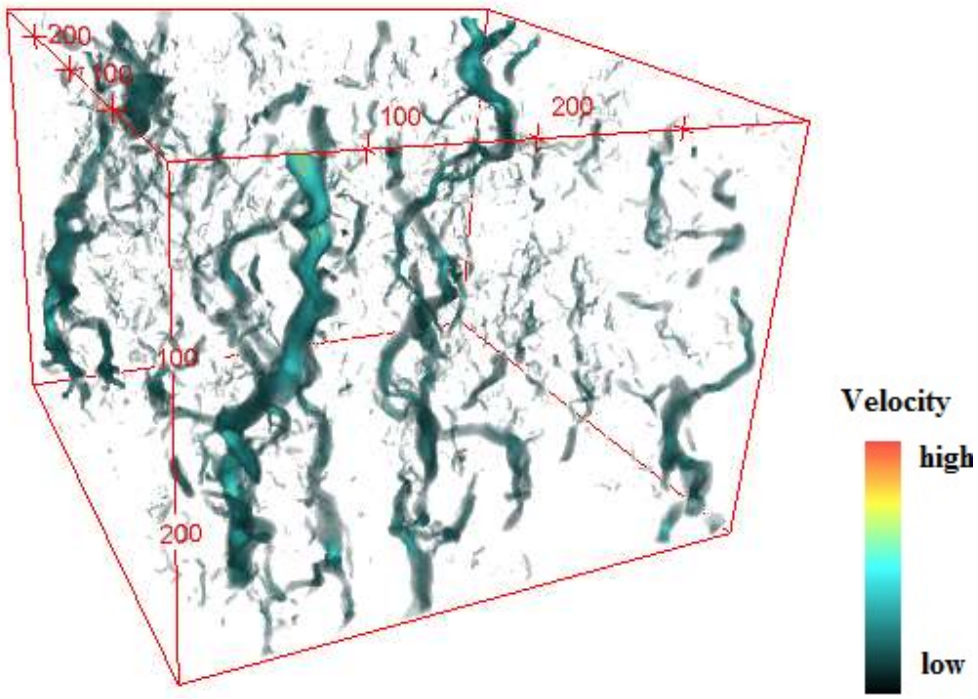

Figure 30: Flow velocity distribution at pH 7 and polymer dosage 250 g/t.

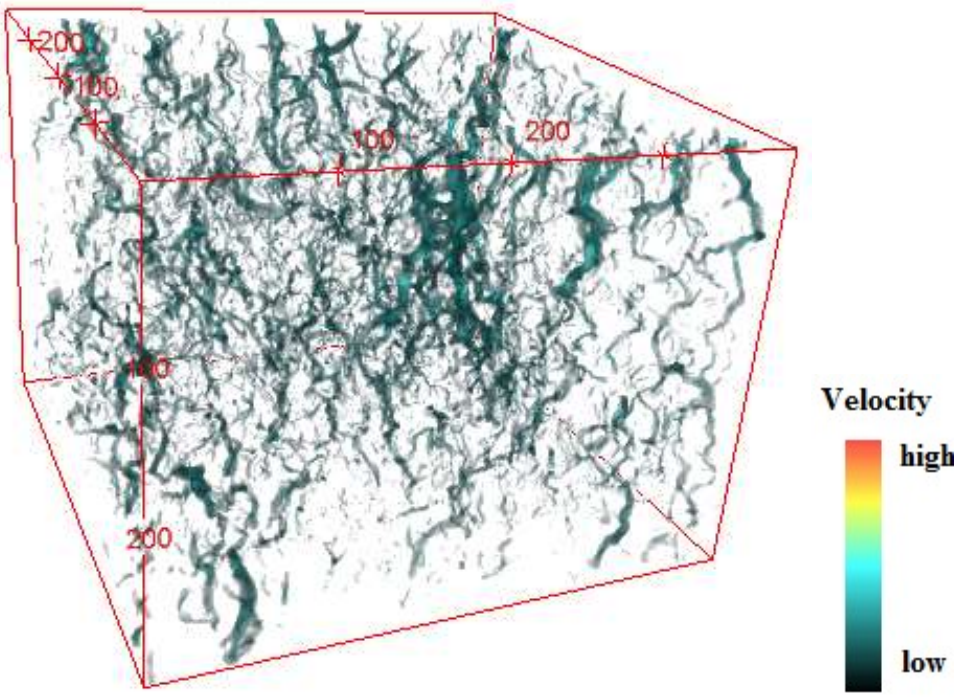

Figure 31: Flow velocity distribution at pH 8 and polymer dosage 250 g/t.

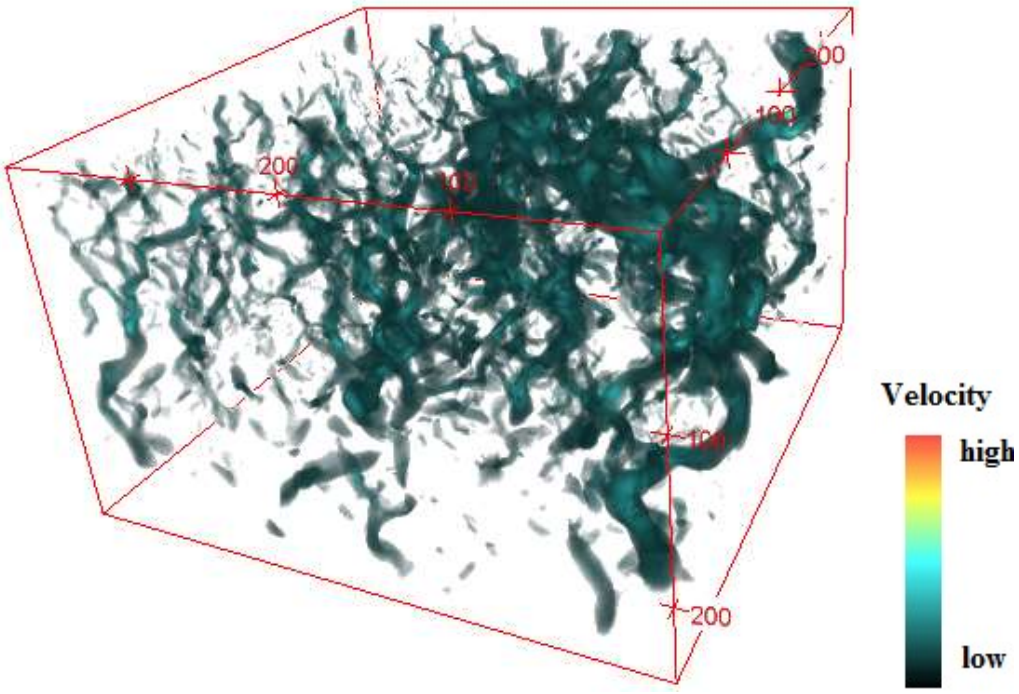

Figure 32: LBM-simulated velocity distribution through a flocculated kaolinite sediment at polymer dosage 500 g/t and pH 6.

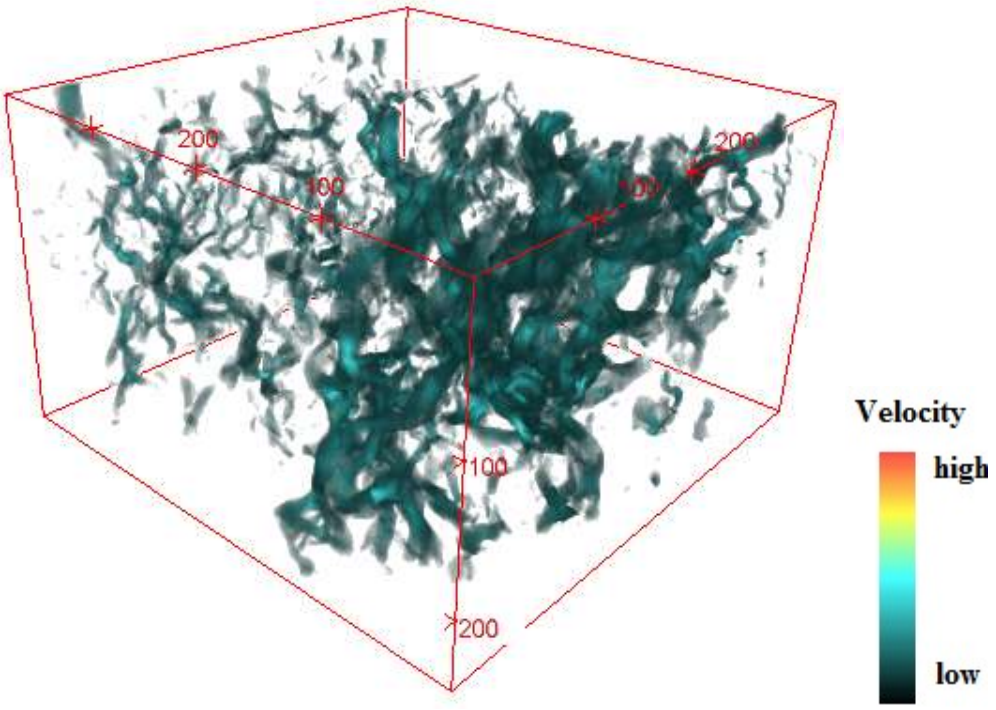

Figure 33: LBM-simulated velocity distribution through a flocculated kaolinite sediment at polymer dosage 500 g/t and pH 7.

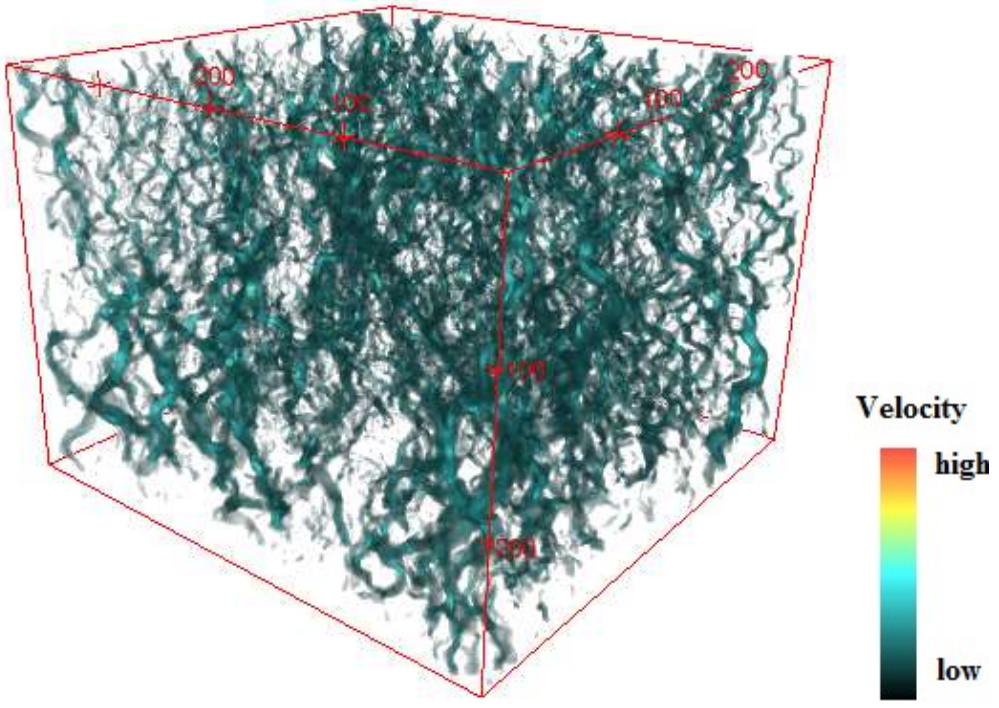

Figure 34: LBM-simulated velocity distribution through a flocculated kaolinite sediment at polymer dosage 500 g/t and pH 8.

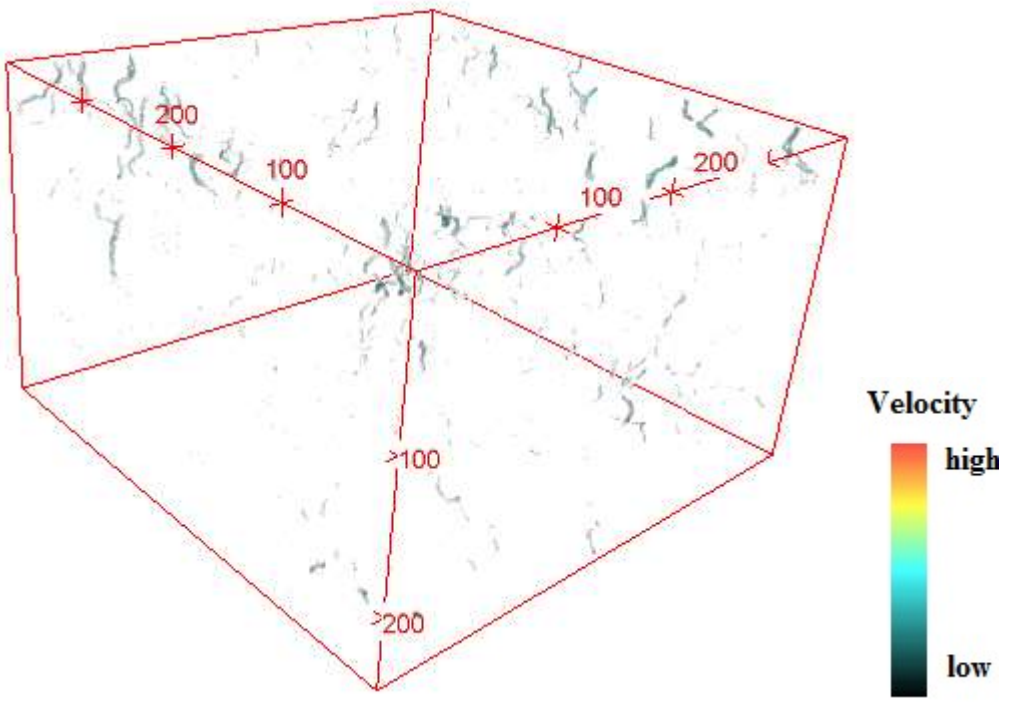

Figure 35: LBM-simulated velocity distribution through a flocculated kaolinite sediment at polymer dosage 500 g/t and pH 9.

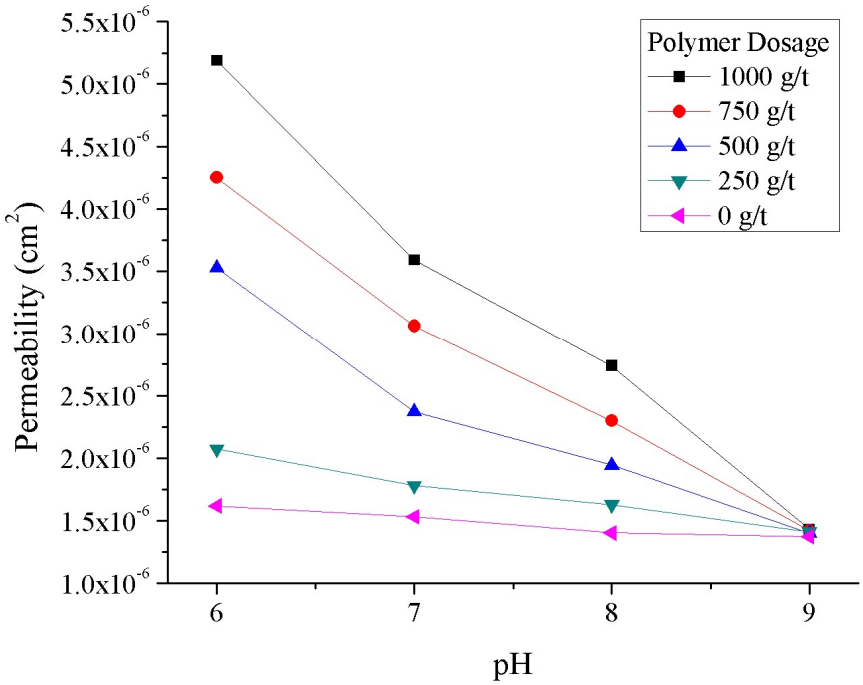

Figure 36: Estimated permeability of flocculated kaolinite sediments for suspension pH values of 6, 7, 8, and 9 for polymer dosages of 0, 250, 500, 750, and 1000 g/t of kaolinite.

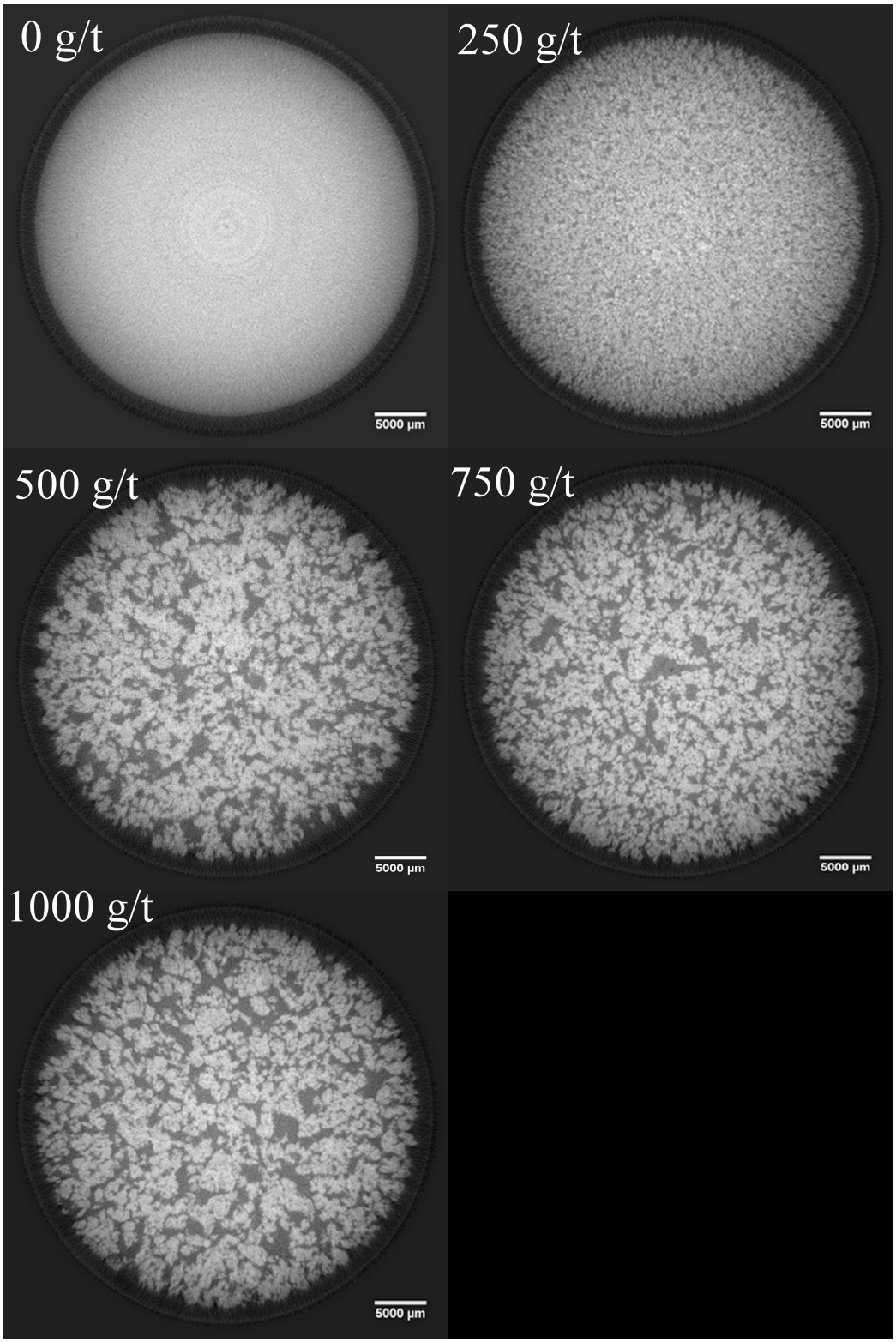

Figure 37: Cross-sectional images at the same depth for kaolinite samples at pH 6 and polymer dosages 0, 250, 500, 750, and 1000 g/t of kaolinite.

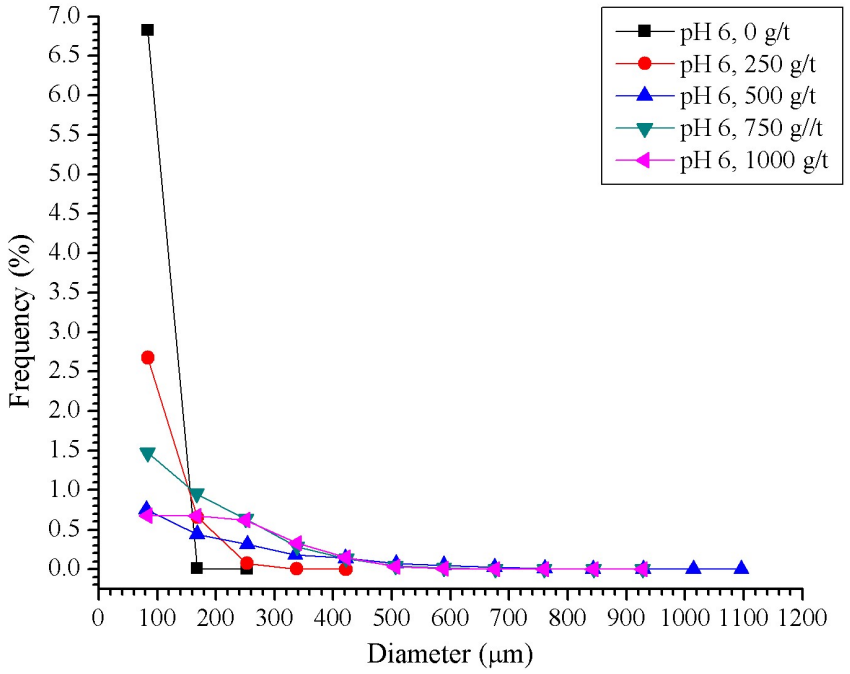

Figure 38: Pore diameter distribution at pH 6.

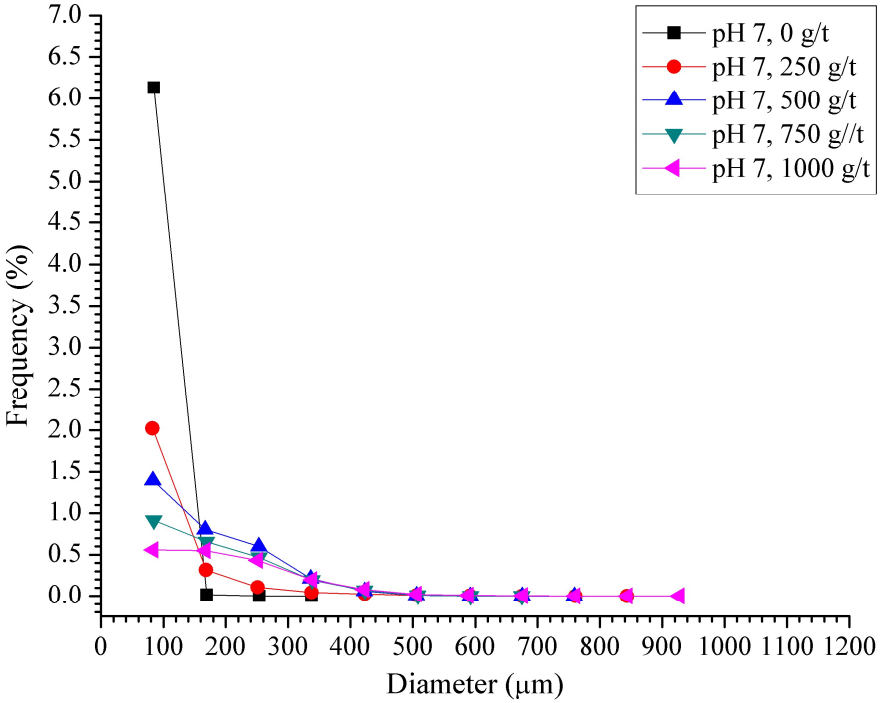

Figure 39: Pore diameter distribution at pH 7.

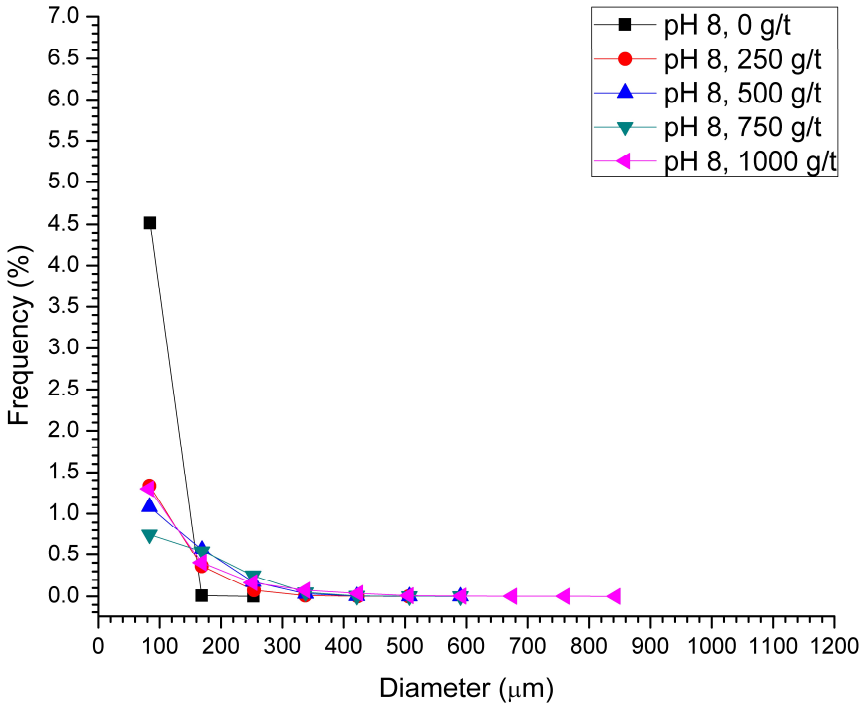

Figure 40: Pore diameter distribution at pH 8.

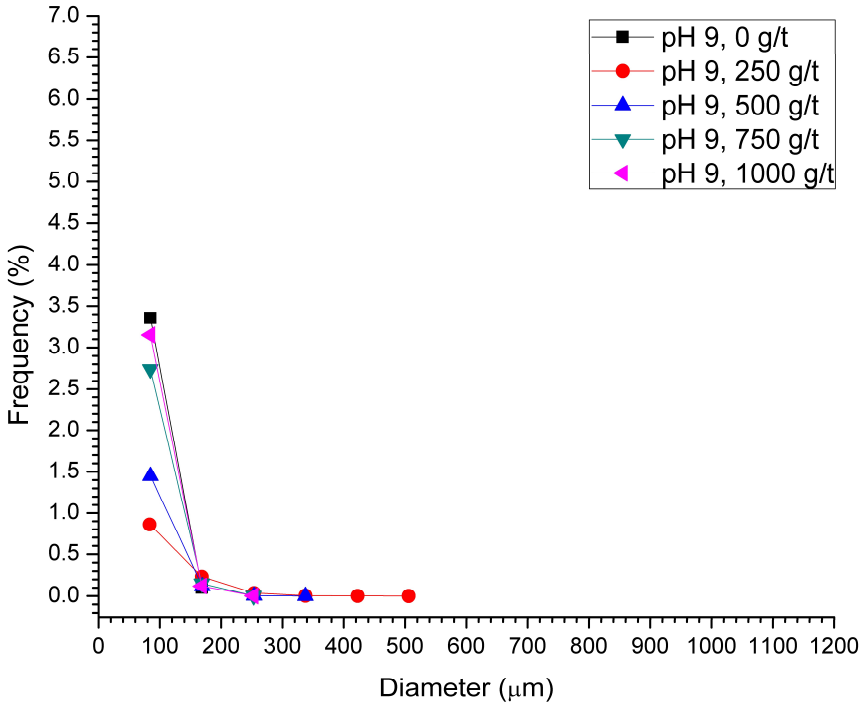

Figure 41: Pore diameter distribution at pH 9.

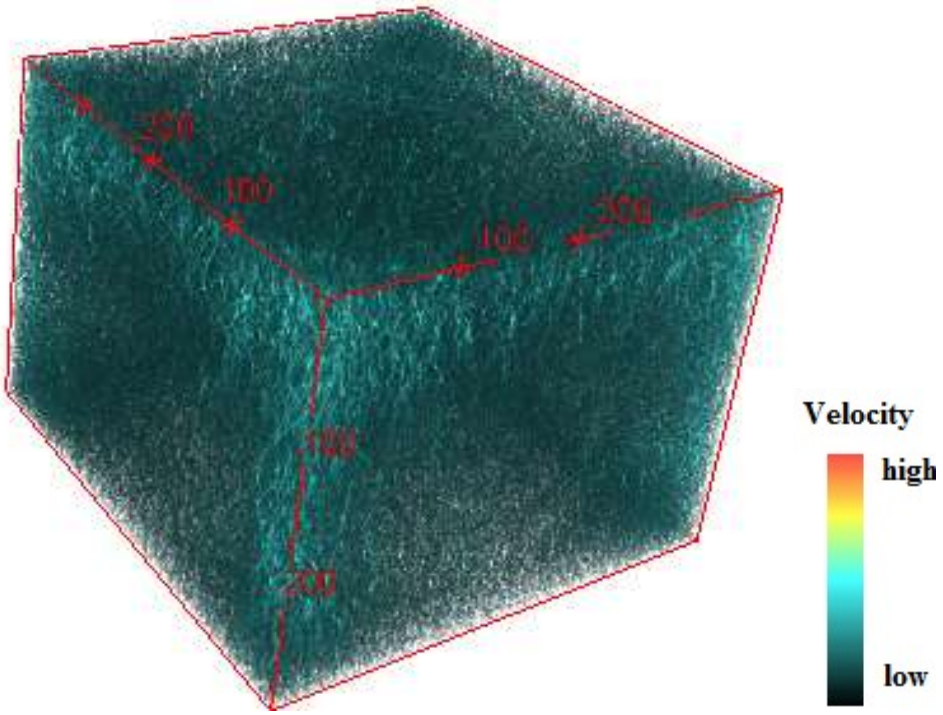

Figure 42: LBM-simulated velocity distribution through a flocculated kaolinite sediment at pH 6 without polymer addition.

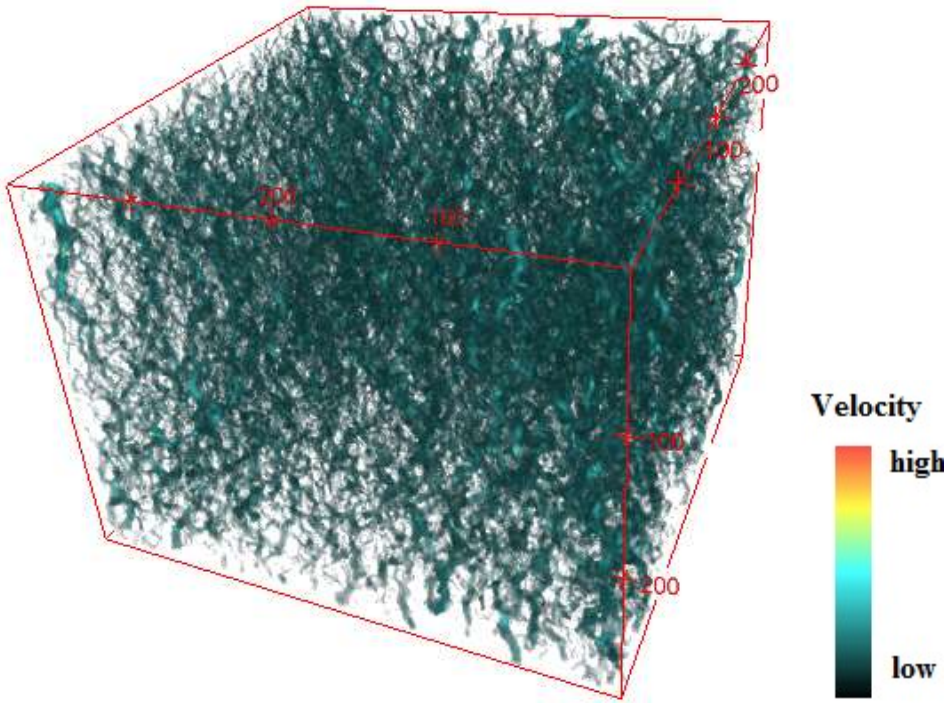

Figure 43: LBM-simulated velocity distribution through a flocculated kaolinite sediment at pH 6 and polymer dosage 250 g/t.

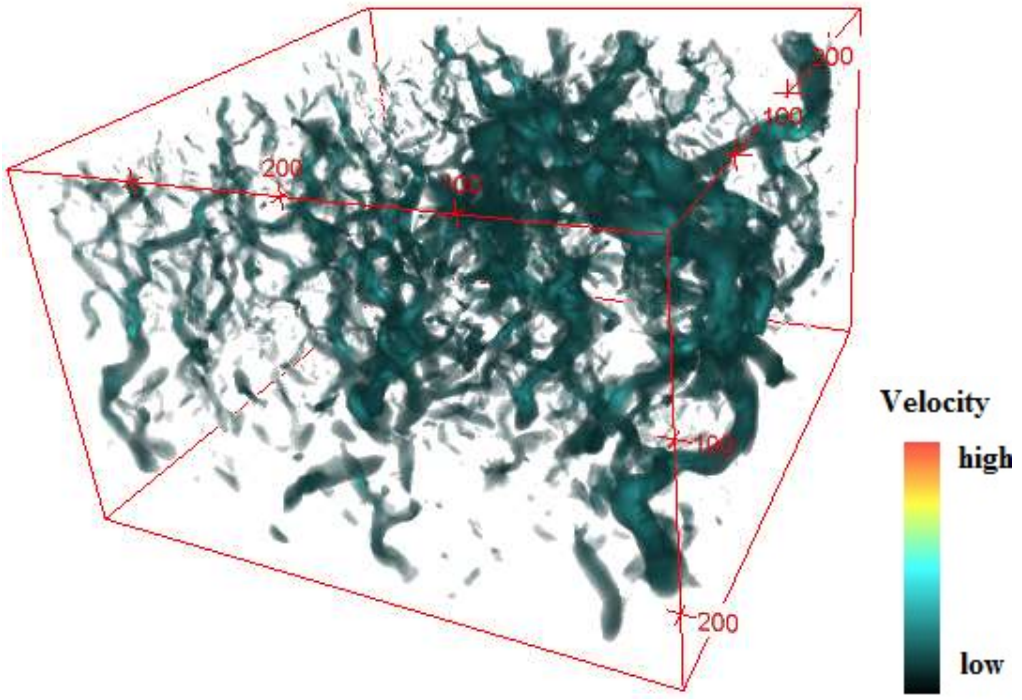

Figure 44: LBM-simulated velocity distribution through a flocculated kaolinite sediment at pH 6 and polymer dosage 500 g/t.

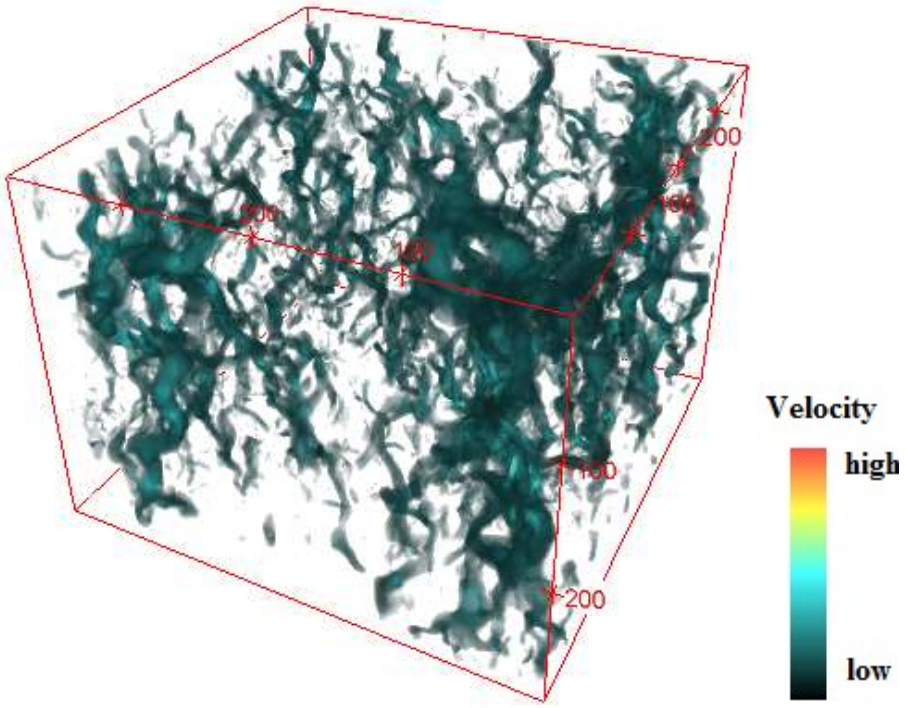

Figure 45: LBM-simulated velocity distribution through a flocculated kaolinite sediment at pH 6 and polymer dosage 750 g/t.

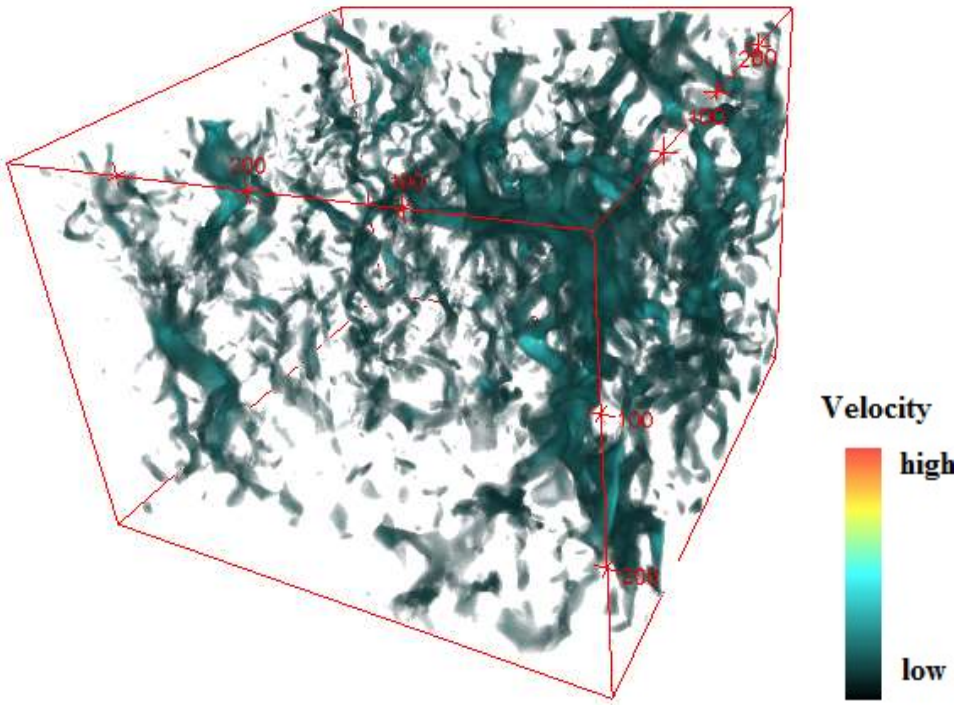

Figure 46: LBM-simulated velocity distribution through a flocculated kaolinite sediment at pH 6 and polymer dosage 1000 g/t.

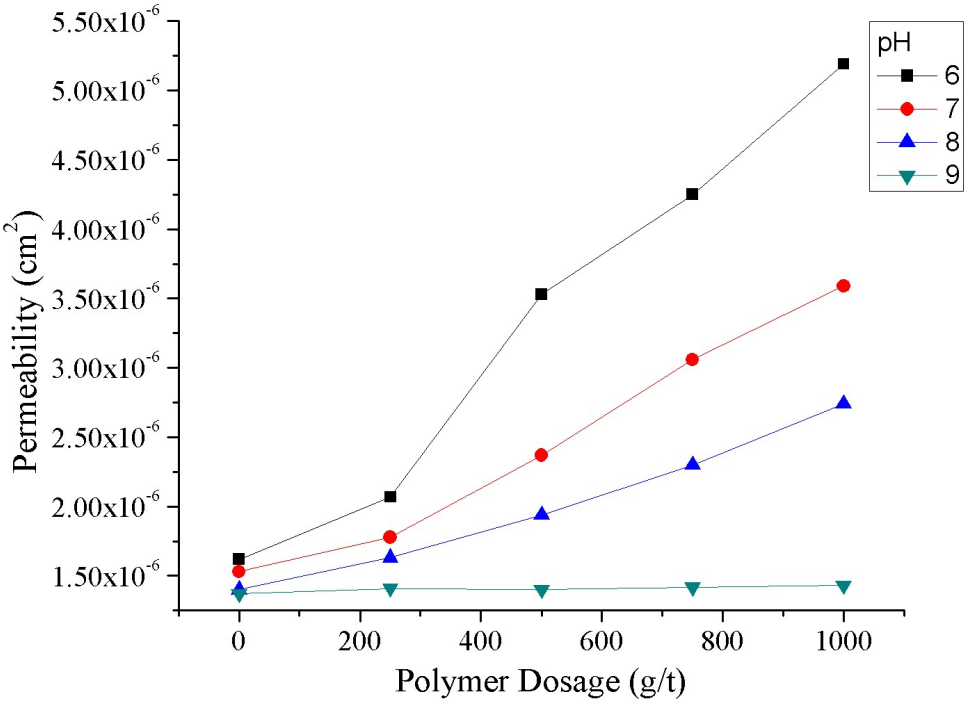

Figure 47: Estimated permeability of flocculated kaolinite sediments as a function of polymer dosage (0, 250, 500, 750, 1000 g/t of kaolinite) at selected pH values.

Table 3: Estimated permeability (cm^2) of flocculated kaolinite sediments in a gravitational field.

	Permeability (cm^2)				
Polymer Dosage (g/t)	0	250	500	750	1000
pH 6	1.62E-06	2.07E-06	3.53E-06	4.25E-06	5.19E-06
pH 7	1.53E-06	1.78E-06	2.37E-06	3.06E-06	3.59E-06
pH 8	1.40E-06	1.63E-06	1.94E-06	2.30E-06	2.74E-06
pH 9	1.37E-06	1.41E-06	1.40E-06	1.42E-06	1.43E-06

CHAPTER 5

SEDIMENT STRUCTURES IN A CENTRIFUGAL FIELD

This chapter presents centrifugation test results regarding consolidation of flocculated kaolinite sediments as affected by centrifugal forces and centrifugation time.

5.1 Effects of Centrifugal Force

The centrifugal force is proportional to the square of frequency of rotation. This thesis explored three levels of centrifugal force within the capacity of the centrifuge. The tests on flocculated kaolinite in a centrifugal field explored centrifugal forces and centrifugation time while keeping the polymer dosage at 1000 g/t and suspension pH at 6. All the tests used the same batch of kaolinite samples. Table 4 lists the frequency used and the corresponding G-Factor. The effect of centrifugal force for 2 minutes of centrifugation was to shrink the channels and release water. Figure 48 presents cross-sectional area images of flocculated kaolinite sediments at the same depth for different centrifugal forces. From a to c, the frequency increases while the centrifugation time is kept constant at two minutes. There are still several large water channels that are several microns in diameter as shown in image a, while images b and c have similar and smaller water channels that are less than a few hundred microns in diameter. It seems that at low centrifugal forces, the compactness of the sediment is highly affected by the centrifugal forces applied, and after reaching a certain G-Factor value a further increase in centrifugal force does not compact

the sediment further. In this case, the compactness of sediment in images b and c are quite similar while the sediment in image a is much more porous.

Figures 49 to 51 show the LB-simulated fluid flow through the flocculated kaolinite sediment centrifuged with a centrifugation time of 2 minutes and at three different G-Factors. Apparently, one can observe that larger flow channels and higher flow velocity show up in lower G-Factor conditions (Figure 49). Also, Figure 50 and Figure 51 have similar small fluid flow channels.

The estimated permeability plotted in Figure 52 and listed in Table 5 display the estimated permeability of flocculated kaolinite in a centrifugal field under various centrifugal forces and confirm the trend that as the G-Factor increases of the permeability of the flocculated kaolinite sediment decreases. Moreover, further increases of the centrifugal force will not enhance the permeability much more after the G-Factor reaches 688 in this case. The centrifuge pushes solid and liquid toward the bottom of the centrifuge tube with centrifugal forces proportional to the mass of solid and liquid. In this case the flocculated kaolinite sediments experienced higher centrifugal force, therefore, moved closer to the bottom of the tube. The liquid phase moves in the opposite direction (relative to the motion of the solid) and forms channels on its way out of the sediments. The pore pressure inside kaolinite sediments is proportional to the centrifugal forces applied and increments in centrifugal forces increase the pore pressure, squeeze out water, and eventually shrink the channels. When centrifugal forces are applied, most of the channel sizes might be less than the voxel resolution (26.33 microns) and, therefore, are not considered in the analysis. At this level of centrifugal force a large number of fine channels that are less than a voxel in diameter are expected to exist in the sediments. Also, the flow

channels are different and unknown because of the resolution limitation. Better voxel resolution is needed to provide accurate estimation of permeability.

5.2 Effects of Centrifugation Time

Experimental results for sedimentation/consolidation of flocculated kaolinite in a centrifugal field considered the centrifugation time while keeping the polymer dosage at 1000 g/t and suspension pH at 6. All the experiments used the same batch of kaolinite samples. The cross-sectional images shown in Figure 53 present the effect that centrifugation time has on the sediment consolidation. From images a to d, the centrifugation time increases from 2 minutes to 8 minutes by increments of 2 minutes while the centrifugal G-Factors are kept constant at 172 G. When compared to image a, images b to d have similar channel sizes that are much smaller than the channel sizes found for image a. Starting at 4 minutes, further increases in centrifugation time does not further compact the sediment. However, from 2 minutes to 4 minutes one can find that the water channels shrink greatly.

Figures 54 to 57 show the LB-simulated fluid flow through the flocculated kaolinite sediment centrifuged at a G-Factor of 172 G and four different centrifugation times. The color bar shown on the right side of each image represents the velocity. The color changes from black to red as the flow velocity increases. The flow velocity for a centrifugation time of 2 minutes is dominated by blue with some higher velocities shown in yellow. Three-dimensional images for the water channels at the other three centrifugation times are similar. They mainly have dark gray color for low flow velocity with some higher flow channels shown in blue.

The estimated permeability plotted in Figure 58 confirms the trend that as the

centrifugation time increases the permeability of the flocculated kaolinite sediment decreases. Moreover, further increase in the centrifugal force will not enhance the permeability much more after the centrifugation time reaches 4 minutes.

Table 6 presents the estimated permeability of flocculated kaolinite sediments in a centrifugal field for selected centrifugation times. Permeability for centrifugation time 4, 6, and 8 minutes are similar. The reason might be the limitation of the voxel resolution. For centrifugation tests the voxel size is 26.33 microns. Channel sizes are expected to be small with centrifugal forces applied. Channel sizes less than a voxel will not be shown in the image and counted. When the centrifugation time is larger than 2 minutes, channel sizes in the sediments are expected to shrink further.

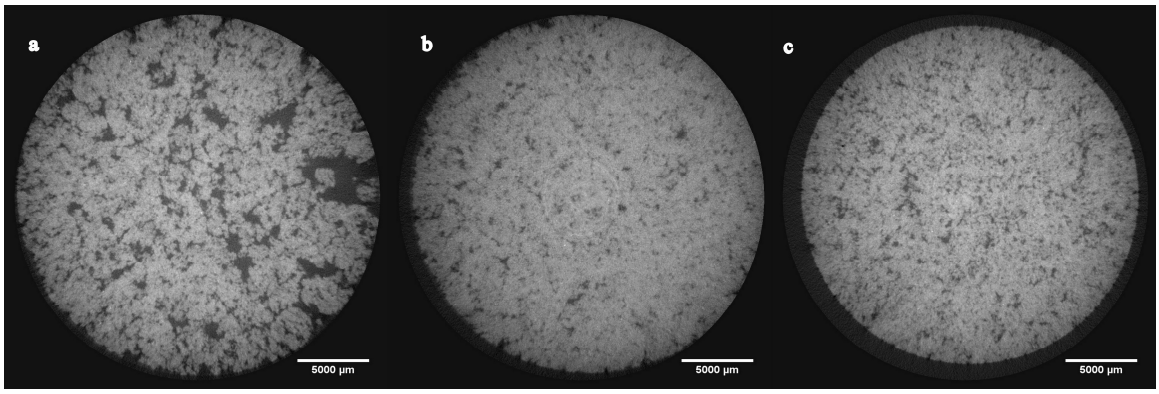

Figure 48: Cross-sectional views of centrifuged kaolinite at increasing G-Factors: (a) 172 G, (b) 688 G, (c) 1547 G.

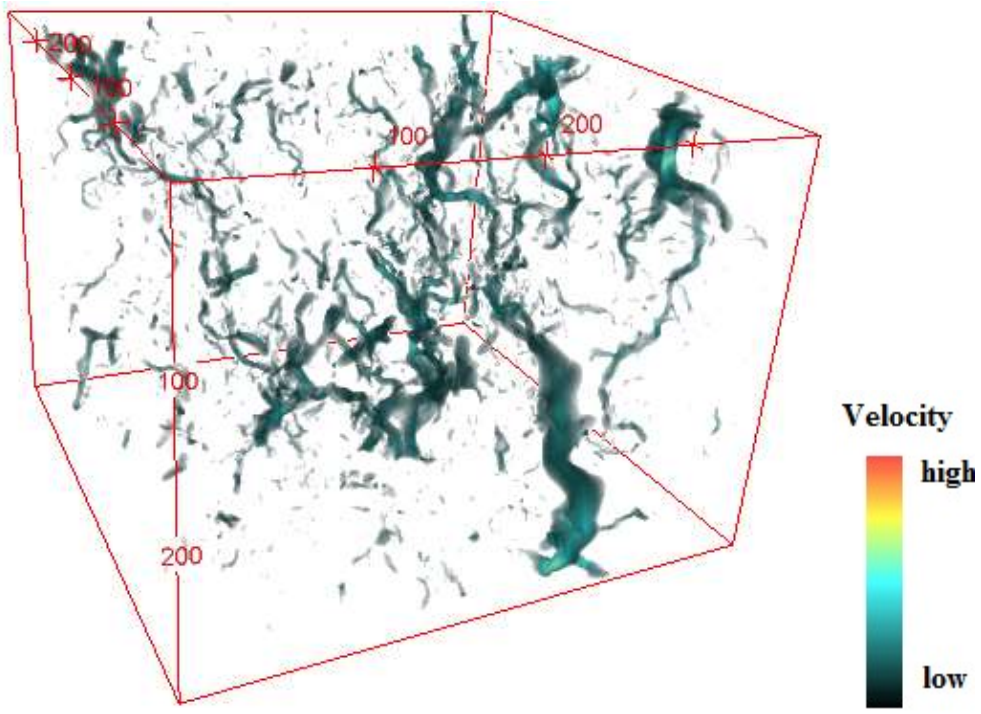

Figure 49: LBM-simulated velocity distribution through a flocculated kaolinite sediment at 172 G-Factor and centrifugation time 2 minutes.

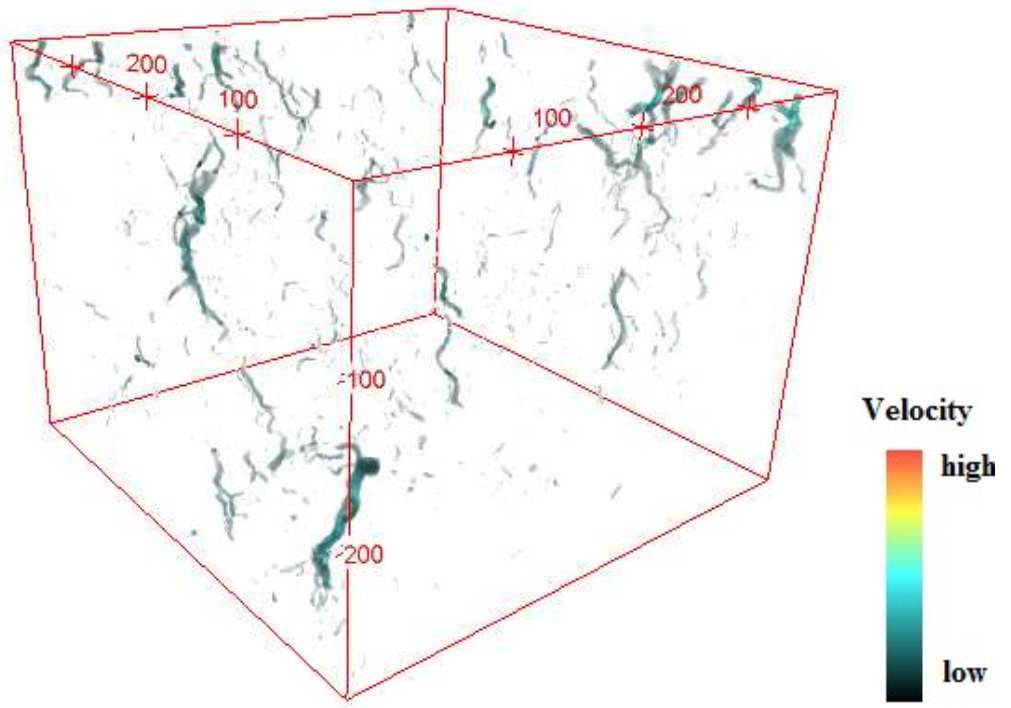

Figure 50: LBM-simulated velocity distribution through a flocculated kaolinite sediment at 688 G-Factor and centrifugation time 2 minutes.

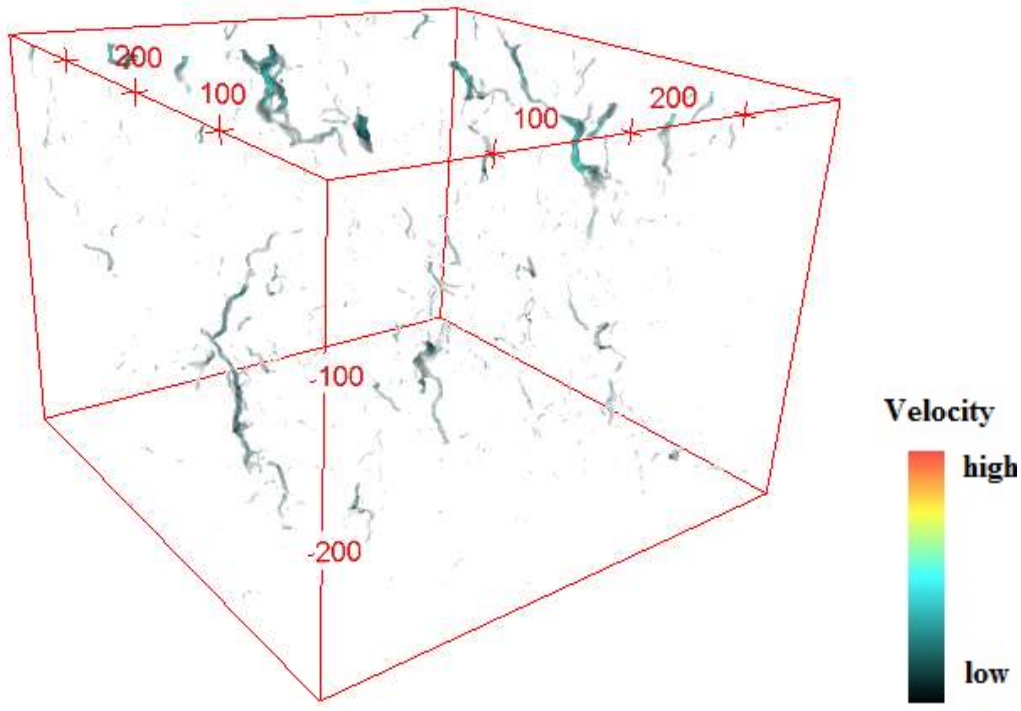

Figure 51: LBM-simulated velocity distribution through a flocculated kaolinite sediment at 1547 G-Factor and centrifugation time 2 minutes.

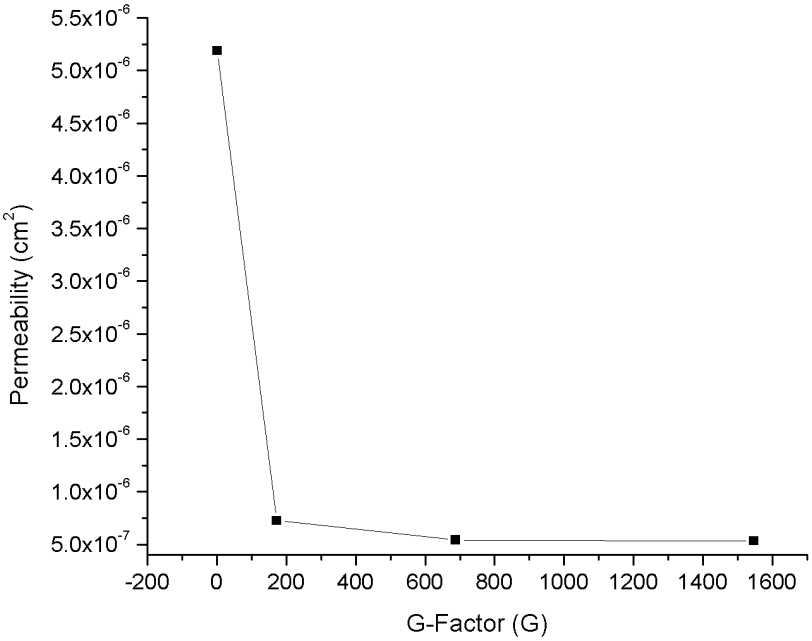

Figure 52: Estimated permeability of centrifuged and flocculated kaolinite sediments at G-Factor 1, 172, 688, and 1547.

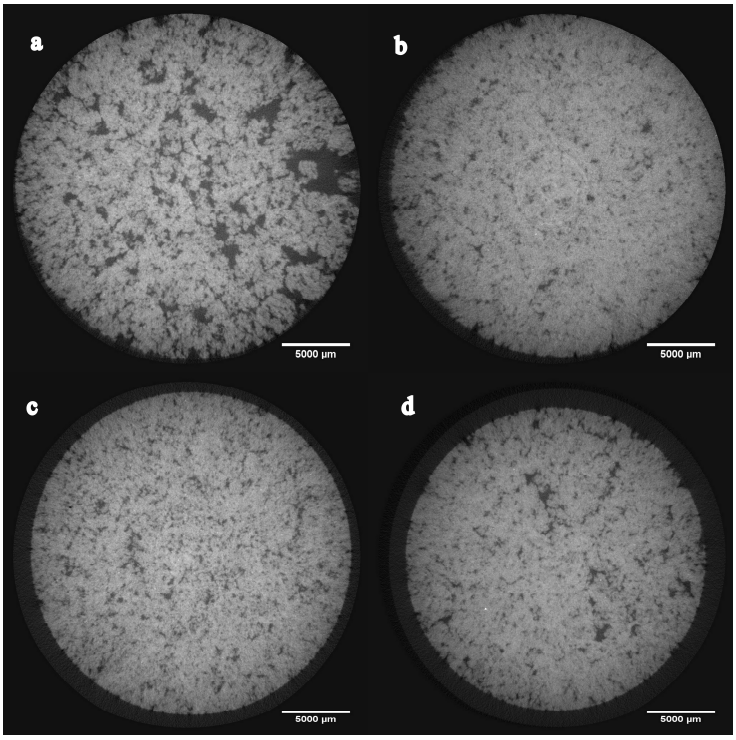

Figure 53: Cross-sectional views of centrifuged flocculated kaolinite sediment at G-Factor 172 and increasing centrifugation times: (a) 2, (b) 4, (c) 6, and (d) 8 minutes.

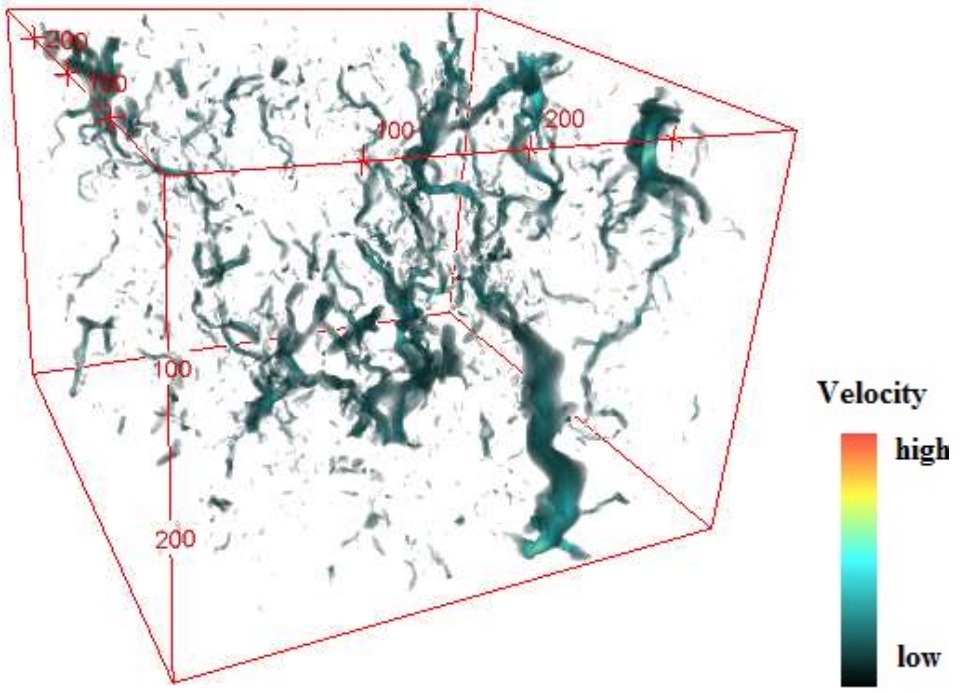

Figure 54: LBM-simulated velocity distribution through a flocculated kaolinite sediment at G-Factor 172 and centrifugation time 2 minutes.

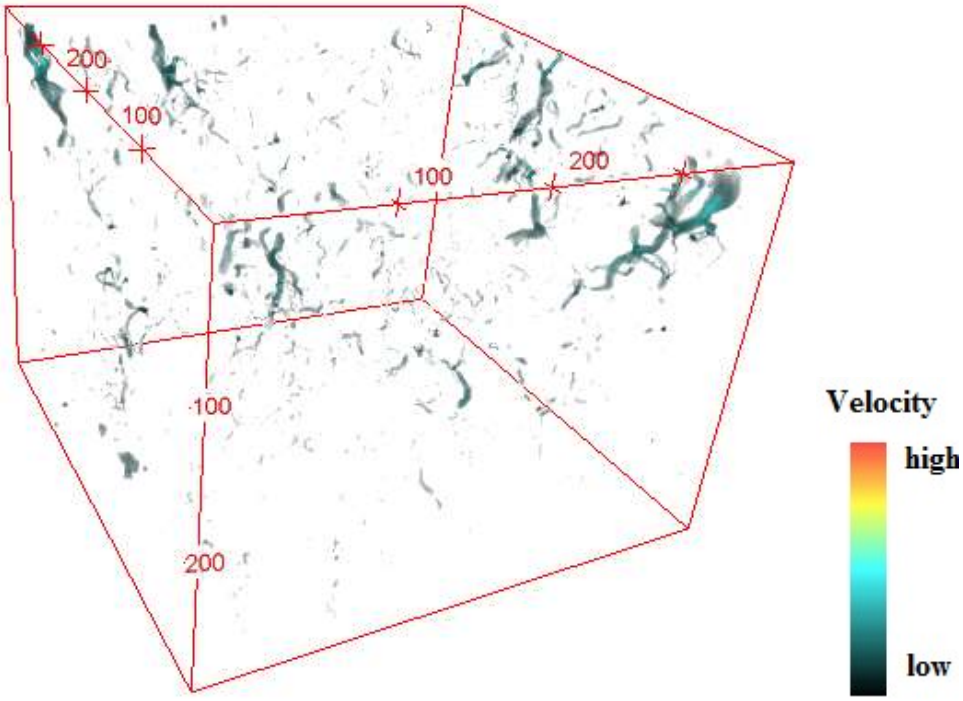

Figure 55: LBM-simulated velocity distribution through a flocculated kaolinite sediment at G-Factor 172 and centrifugation time 4 minutes.

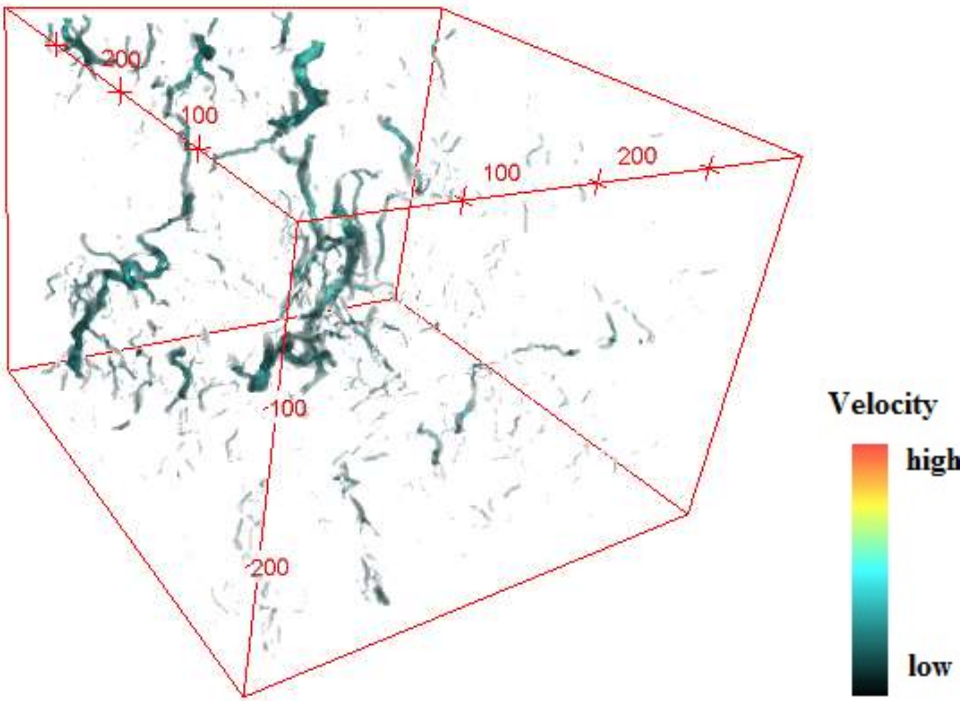

Figure 56: LBM-simulated velocity distribution through a flocculated kaolinite sediment at G-Factor 172 and centrifugation time 6 minutes.

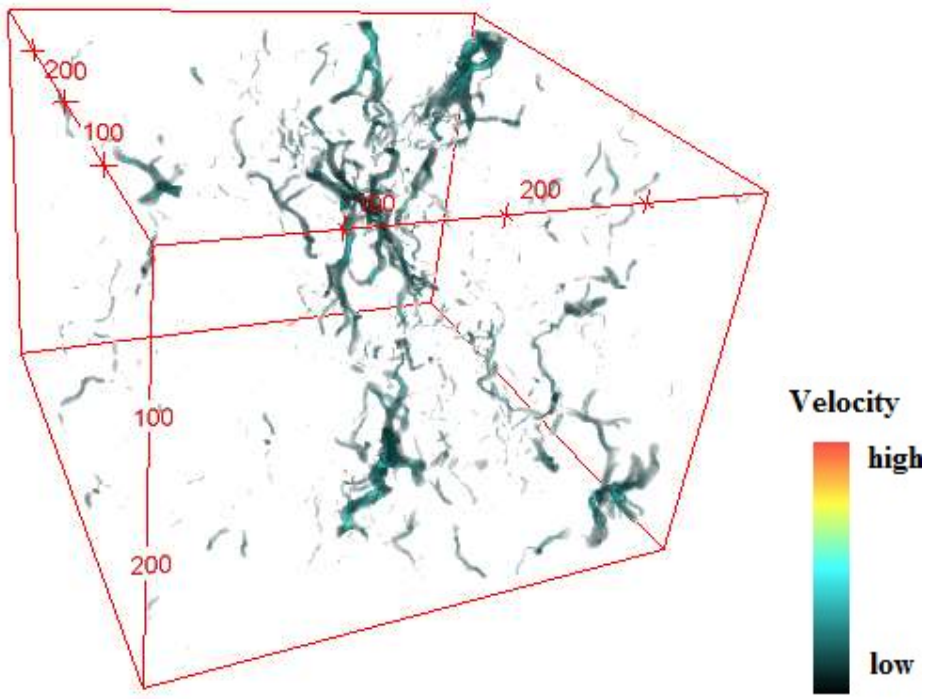

Figure 57: LBM-simulated velocity distribution through a flocculated kaolinite sediment at G-Factor 172 and centrifugation time 8 minutes.

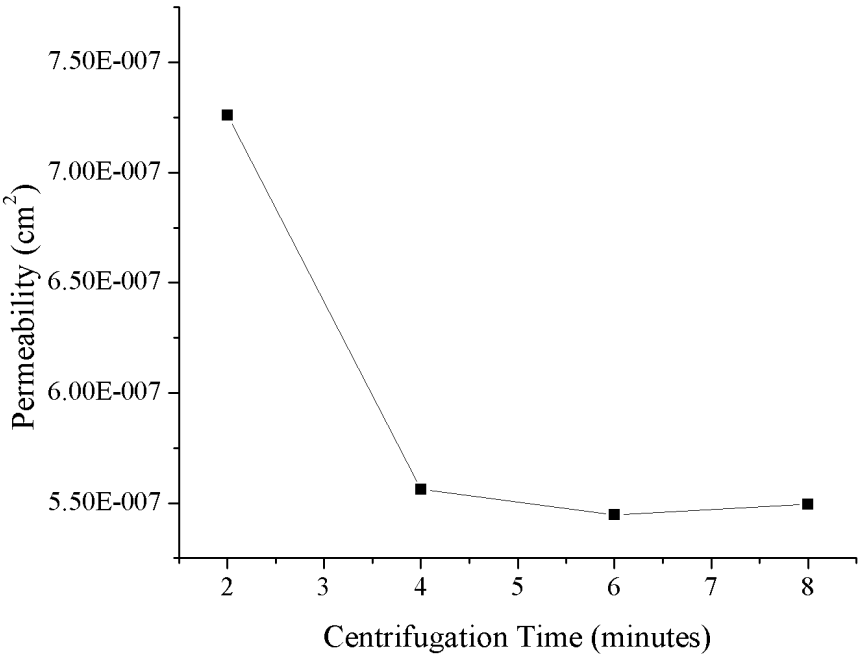

Figure 58: Estimated permeability of flocculated kaolinite sediments centrifuged for 2, 4, 6, and 8 minutes at G-Factor 172.

Table 4: Frequency and corresponding G-Factor used to study consolidation of the flocculated kaolinite sediment.

Frequency (rpm)	1225	2450	3675
G-Factor (g)	172	688	1547

Table 5: Estimated permeability (cm^2) of flocculated kaolinite sediment for different centrifugal forces.

G-Factor (g)	172	688	1547
Permeability (cm^2)	7.26E-07	5.40E-07	5.33E-07

Table 6: Estimated permeability (cm^2) of flocculated kaolinite sediment for selected centrifugation times.

Centrifugation time (minutes)	2	4	6	8
Permeability (cm^2)	7.26E-07	5.56E-07	5.45E-07	5.49E-07

CHAPTER 6

SUMMARY, CONCLUSIONS, AND RECOMMENDATIONS

6.1 Summary and Conclusions

Flocculated kaolinite samples were sedimented/consolidated in both a gravitational field and a centrifugal field. The sediment samples were scanned using high resolution X-ray microtomography (HRXMT) and the 3D images were analyzed using image processing software to define the pore network structure. Based on the 3D pore network structure, the permeabilities were estimated from LB simulation. The estimated permeability of flocculated kaolinite sediment in a gravitational field is about ten times as large as the permeability in a centrifugal field.

The permeability of flocculated kaolinite sediments in a gravitational field increases with increasing polymer dosage. The permeability of flocculated kaolinite sediments in a gravitational field decreases as the suspension pH increases. Permeability ranged from 1.37E-06 to 5.19 E-06 cm^2. These results are of the same magnitude as the permeability of flocculated mature fine tailings (Alberta oil sand tailings) estimated using the same procedures and conditions.

The permeability of flocculated kaolinite sediments in a centrifugal field decreases as the centrifugal force increases. The permeability of flocculated kaolinite sediments in a centrifugal field decreases as the centrifugation time increases. Permeability ranged from 5.33E-07 to 7.26 E-07 cm^2 depending on the centrifugation force and time of centrifugation.

Due to the limitation of voxel resolution, increments in centrifugal forces or centrifugation time did not change the measured permeability of the sediments much, as at high centrifugal forces and long centrifugation time narrow channels less than one voxel size are more common.

Due to limitation of the voxel resolution used in this thesis, channels sizes that are less than 1 voxel cannot be counted which could be the main reason why permeability of flocculated kaolinite sediments measured almost the same with both no polymer addition and high suspension pH conditions.

Fundamental understanding of flocculated kaolinite sediments at the pore-scale level is important for developing sustainable tailings management for many mineral processing operations including phosphate tailings in Florida and oil sand mature fine tailings in Alberta, Canada. Both centrifugation and polymer application can improve kaolinite flocculation and consolidation. The main contributions from this research are as follows:

- Coupling HRXMT measurements with image processing procedures and LBM to simulate fluid flow through flocculated kaolinite sediments and thereby estimate permeability.
- Identification of operating conditions for improved consolidation of flocculated kaolinite, including centrifugation.

6.2 Recommendations

Based on the results of this thesis research the following recommendations for future research are made.

1) Examine kaolinite sediment structure at higher resolution, calculate permeability

from simulation, and compare estimated permeability from simulation to experimental values.

2) Consider the effect of different polymer properties (polymer dosage, molecular weight, charge density) on structures to identify conditions for improved sedimentation and consolidation.
3) Evaluate the consolidation of industrial tailings using the techniques developed in this thesis research.

REFERENCES

[1] Carolina Motta, Jonathan Bryan, and Apostolos Kantzas: in *10th Int. Mine Water Assoc. Congr.*, Karlovy, Czech Republic, 2008.

[2] Fine Tailings Fundamentals Consortium FTFC: *Advances in Oil Sands Tailings Research*, Alberta Department of Energy, Oil Sands and Research Division, 1995.

[3] Jacob Masliyah, Jan Czarnecki, and Zhenghe Xu: *Handbook on Theory and Practice of Bitumen Recovery from Athabasca Oil Sands*, Kingsley Knowledge Publishing Alberta, Canada, 2011,pp. 391-93.

[4] Chun Zhang: M.S. University of Alberta, 1994.

[5] Vishal Gupta, Marc A. Hampton, Anh V. Nguyen, and Jan D. Miller: *J. Colloid Interface Sci.*, 2010, vol. 352, pp. 75–80.

[6] Jing Liu, Linda Sandaklie-Nikolova, Xuming Wang, and Jan D. Miller: *J. Colloid Interface Sci.*, 2014, vol. 420, pp. 35–40.

[7] R.K. Schofield and H.R. Samson: *Discuss. Faraday Soc.*, 1954, vol. 18, pp. 135–45.

[8] H. Van Olphen: *An Introduction to Clay Colloid Chemistry, for Clay Technologists, Geologists, and Soil Scientists.*, New York, 1977.

[9] J. Lyklema: *Fundamentals of Interface and Colloid Science*, San Diego: Academic Press, 1991.

[10] Vishal Gupta: Ph.D., University of Utah, 2011.

[11] Vishal Gupta and Jan D. Miller: *J. Colloid Interface Sci.*, 2010, vol. 344, pp. 362–71.

[12] Xihui Yin: Ph.D., University of Utah, 2012.

[13] Jing Liu: Ph.D., University of Utah, 2015.

[14] Jing Liu, Chen-Luh Lin, and Jan D. Miller: *Int. J. Miner. Process.*, 2015, vol. 145, pp. 38–47.

[15] M.S. Nasser and A.E. James: *Sep. Purif. Technol.*, 2006, vol. 52, pp. 241–52.

[16] Tridib Tripathy and Bhudeb Ranjan De: *J. Phys. Sci.*, 2006, vol. 10, pp. 93–127.

[17] Patience Mpofu, Jonas Addai-Mensah, and John Ralston: *Int. J. Miner. Process.*, 2003, vol. 71, pp. 247–68.

[18] Sushant Agarwal: Ph.D., West Virginia University, 2002.

[19] A. Demoz, V. Munoz, and R. Mikula: in *Second Int. Oil Sands Tailings Conf.*, 2010, pp. 107–21.

[20] Sungho Kim and Angelica M. Palomino: *Appl. Clay Sci.*, 2009, vol. 45, pp. 270–79.

[21] David A. Laird: *Soil Sci.*, 1997, vol. 162, pp. 826–32.

[22] F. Concha and E.R. Almendra: *Int. J. Miner. Process.*, 1979, vol. 6, pp. 31–41.

[23] Karl Terzaghi: *Theoretical Soil Mechanics*, Wiley Online Library, New York, NY, 1943, pp. 165.

[24] H. El-Shall, B. Moudgil, and M. Bogan: *Miner. Metall. Process.*, 1996, vol. 13, pp. 98–102.

[25] H.S. Coe and G.H. Clevenger: *Trans. AIME*, 1916, vol. 55, pp. 356–84.

[26] R.T. Mishler: *Eng. Min. J*, 1912, vol. 94, pp. 643–46.

[27] G.J. Kynch: *Trans. Faraday Soc.*, 1952, vol. 48, pp. 166–76.

[28] R.E. Gibson, G.L. England, and M.J.L. Hussey: *Géotechnique*, 1967, vol. 17, pp. 261–73.

[29] F. Concha and E.R. Almendra: *Int. J. Miner. Process.*, 1979, vol. 5, pp. 349–67.

[30] ASTM-D-2434-68: *ASTM Int.*, 2006.

[31] Suksun Horpibulsuk, Narongded Yangsukkaseam, Avirut Chinkulkijniwat, and Yan

Jun Du: *Appl. Clay Sci.*, 2011, vol. 52, pp. 150–59.

[32] D. Reid and A. Fourie: in *Proc. Tailings Mine Waste*, Keystone, Colorado, 2012, pp. 14–17.

[33] M. Prodanovic: Ph.D., Stony Brook University, 2005.

[34] Alvaro R. Videla, Chen-luh Lin, and Jan D. Miller: *J. Chinese Inst. Chem. Eng.*, 2008, vol. 39, pp. 117–28.

[35] ImageJ: *IJ 1.46r*, 2003, vol. 9, p. 187.

[36] Mark Hall, Eibe Frank, Geoffrey Holmes, Bernhard Pfahringer, Peter Reutemann, and Ian H. Witten: *ACM SIGKDD Explor. Newsl.*, 2009, vol. 11, pp. 10–18.

[37] Ignacio Arganda-Carreras, Verena Kaynig, Curtis Rueden, Johannes Schindelin, Albert Cardona, and H. Sebastian Seung: *Trainable Weka Segmentation (Fiji),* 2017.

[38] C.L. Lin, A.R. Videla, and J.D. Miller: *Flow Meas. Instrum.*, 2010, vol. 21, pp. 255–61.

[39] R.S. Maier, D.M. Kroll, Y.E. Kutsovsky, H.T. Davis, and R.S. Bernard: *Phys. Fluids*, 1998, vol. 10, pp. 60–74.

[40] T.C. Lee, R.L. Kashyap, and C.N. Chu: *CVGIP Graph. Model. Image Process.*, 1994, vol. 56, pp. 462–78.

[41] Jacob Bear: *Dynamics of Fluids in Porous Media*, American Elsevier, New York, NY, 1972, pp. 143–45.